Economic Geology, v. 110, pp. 631–652

Genesis and Magmatic-Hydrothermal Evolution of the Yangla Skarn Cu Deposit, Southwest China

Jing-jing Zhu,[1,2,†] Ruizhong Hu,[1,†] Jeremy P. Richards,[2] Xianwu Bi,[1] and Hong Zhong[1]

[1] *State Key Laboratory of Ore Deposit Geochemistry, Institute of Geochemistry, Chinese Academy of Sciences, Guiyang 550002, PR China*

[2] *Department of Earth and Atmospheric Sciences, University of Alberta, Edmonton, Alberta T6G 2E3, Canada*

Abstract

The Yangla skarn Cu deposit (150 Mt at 1.03% Cu) is located in the central segment of the Jinshajiang metallogenic belt within the Sanjiang (Three Rivers) region, southwest China. Skarn orebodies are mainly developed between different units of Devonian carbonate and quartz sandstone rocks with stratiform-like shapes, or within the contact zone between granitoids and marbles. Re-Os dating of molybdenite intergrowth with chalcopyrite yielded a well-constrained ^{187}Re-^{187}Os isochron age of 232.0 ± 1.5 Ma with a weighted average age of 231.8 ± 1.3 Ma, both coeval with the related intrusions (233.1 ± 1.4 and 231.0 ± 1.6 Ma at 2σ by zircon U-Pb dating) from our previously published work. Field and textural relationships indicate three hydrothermal stages characterized by assemblages of prograde skarn (pre-ore stage), retrograde skarn and Cu-Fe-Mo-Bi sulfides (main ore stage), and Pb-Zn sulfides associated with calcite and quartz (late ore stage), as well as one supergene stage marked by secondary Cu mineralization (malachite and azurite). Skarns contain garnets with andraditic compositions (Ad_{96} $Gr_{2\sim3}Py_{0\sim1}$) and clinopyroxene (two series: Hd_6Di_{94} and $Hd_{86}Di_{13}Jo_1$) with low Mn/Fe ratios (<0.1), typical of Cu skarn deposits worldwide.

Three stages of fluid evolution were observed by a detailed fluid inclusion study: (1) Early fluids were trapped under two-phase conditions, as evidenced by the coexistence of brine (homogenization temperatures = 560°–600°C, average salinity = 49.4 ± 1.7 wt % NaCl equiv, n = 33) and vapor-rich inclusions in pre-ore stage andradite and diopside (trapped at ~600 bars, or a depth of approximately 2 km assuming lithostatic pressure conditions). (2) Main ore stage fluid inclusions in quartz were also trapped under two-phase conditions (boiling), as identified by the coexistence of vapor- and liquid-rich fluid inclusions; liquid-rich inclusions homogenized between 312° and 389°C (average = 350° ± 24.7°C, n = 20), with salinities of 2.4 to 5.6 wt % NaCl equiv (average = 4.2 ± 0.9 wt % NaCl equiv, n = 13) and a depth of ~2 km (~200 bars, hydrostatic pressure conditions). (3) Late ore stage fluids are represented by inclusions in calcite, characterized by homogenization temperatures ranging from 220° to 290°C (average = 249° ± 27°C, n = 14) and salinities between 2.1 and 8.0 wt % NaCl equiv (average = 4.6 ± 1.5 wt % NaCl equiv, n = 11).

Sulfur isotope compositions of sulfide minerals (pyrite, chalcopyrite, pyrrhotite, and molybdenite) from the main and late ore stage have a narrow range of $\delta^{34}S$ values from –1.9 to 2.6‰, consistent with a magmatic origin. Calcite in the late ore stage has $\delta^{13}C$ values ranging from –3.2 to –5.9‰ and $\delta^{18}O$ from 7.2 to 18.0‰, distinct from the host-rock marble compositions ($\delta^{13}C$ = 1.2–4.3‰, $\delta^{18}O$ = 10.8–23.9‰). When corrected for temperature (250°C, estimated from fluid inclusion analysis in calcites), these calcite data correspond to ore fluid $\delta^{13}C_{fluid}$ values of –2.0 to –4.6‰ and $\delta^{18}O_{fluid}$ values of 0.5 to 11.2‰ (clustering at ~10‰), which are consistent with a magmatic origin.

Lead isotope compositions of sulfides ($^{206}Pb/^{204}Pb$ = 18.273–18.369, $^{207}Pb/^{204}Pb$ = 15.627–15.677, and $^{208}Pb/^{204}Pb$ = 38.445–39.611) are similar to those of the granitic intrusions and sedimentary wall rocks, but distinct from those of basalts ($^{206}Pb/^{204}Pb$ = 18.282–19.133, $^{207}Pb/^{204}Pb$ = 15.564–15.665, and $^{208}Pb/^{204}Pb$ = 38.367–38.942) in the mining area. Taken together, these geologic, geochemical, and isotopic data confirm that Yangla is a typical Cu skarn deposit.

Introduction

The Sanjiang (Three Rivers) metallogenic domain (Fig. 1) is a constituent part of the Tethyan metallogenic belt, and is considered to be one of the most important polymetallic belts in China, hosting numerous ore deposits, including several porphyry and skarn Cu-Au deposits (Mo et al., 1993; Hou et al., 2007; Zaw et al., 2007; Deng et al., 2014). The Yangla Cu deposit (99°06'E, 28°55'N) in the central Sanjiang region is located near the Jinshajiang River, ~100 km northwest of the city of Shangri-la, Yunnan Province (Fig. 1). The potential for Cu mineralization was first recognized by the 18th Brigade of the Yunnan Bureau of Geology and Mineral Resources in 1965; however, commercial production by the Yunnan Copper (Group) Corporation did not begin until 2007, mostly due to problems posed by the rugged environment. Since 2007, it has been the largest Cu deposit mined in the Sanjiang region, containing measured and indicated resources of 150 million tonnes of ore grading 1.03% copper.

Over the past two decades, several studies have been carried out on the Yangla Cu deposit, most of which were published in Chinese; however, many issues, including its genesis, are still debated. A number of authors believe it has a syngenetic exhalative or volcanogenic origin because the orebodies generally show stratigraphic control (e.g., Y.F. Lu et al., 1999; J. Pan et al., 2000, 2001; Yang, 2012). Several authors have proposed a terminology of "stratiform skarn," indicative of an exhalative-sedimentary skarn origin unrelated to an intrusive contact (Y.F. Lu et al., 1998; Zhan et al., 1998; J. Zhu et al., 2011). In contrast, other researchers think that

†Corresponding authors: e-mail, zhujingjing-1103@163.com; huruizhong@vip.gyig.ac.cn

Submitted: April 17, 2014
Accepted: September 11, 2014

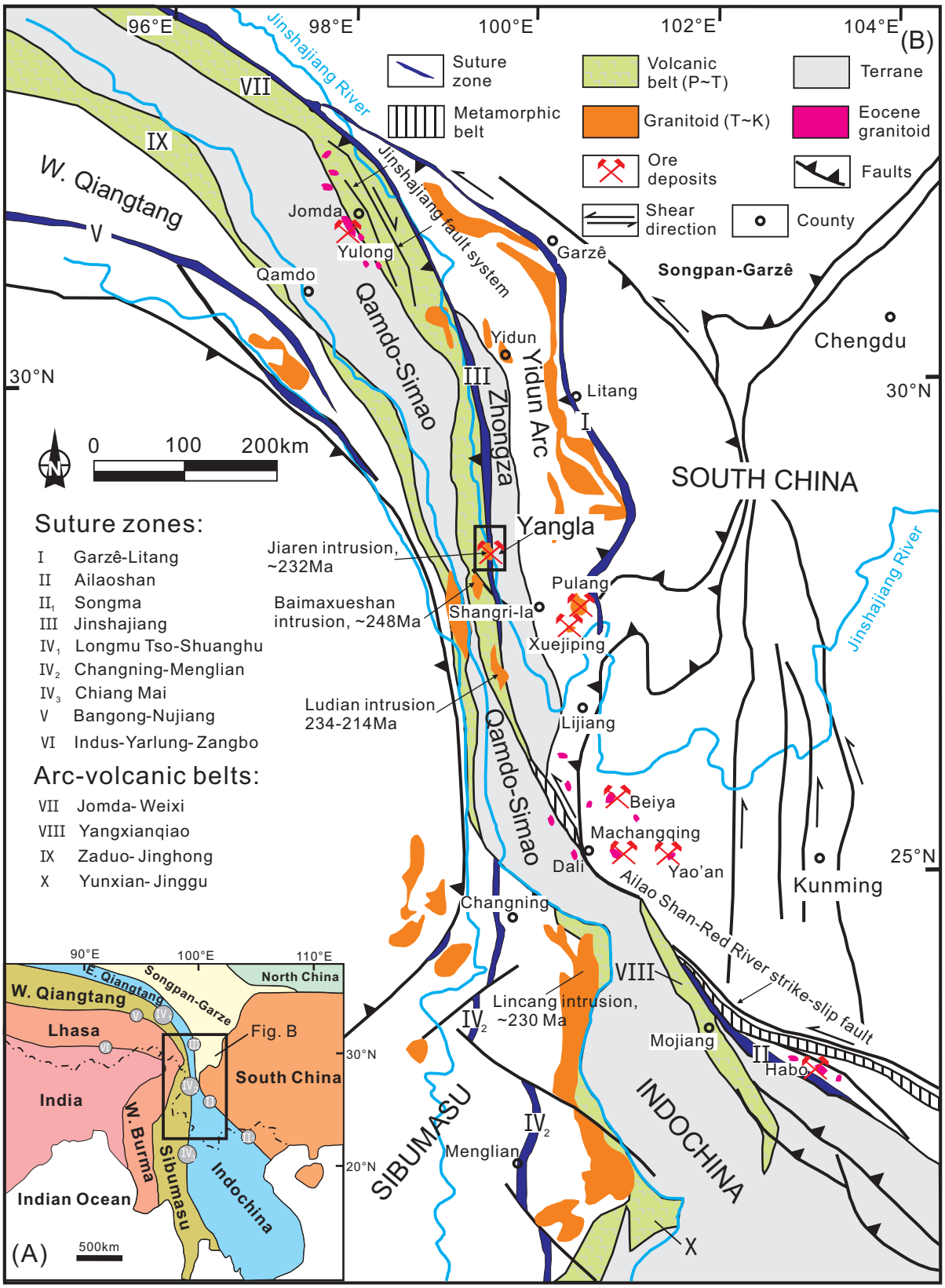

FIG. 1. (A) Distribution of principal continental blocks and sutures of southeast Asia (modified from Metcalfe, 2006, 2013). (B) Tectonic framework of the Sanjiang region in southwest China showing the major terranes, suture zones, arc volcanic belts, and locations of the Yangla Cu deposit and other major porphyry Cu deposits (modified from Zi et al., 2012a; Deng et al., 2014). The ages of the Ludian and Baimaxueshan batholiths are both from Zi et al. (2012c).

Yangla is a skarn deposit genetically associated with granitic intrusions (e.g., Qu et al., 2004; J.-J. Zhu et al., 2011; Chen et al., 2013). The former hypothesis suggests that the deposit is syngenetic and generated by submarine exhalative or synvolcanogenic processes (e.g., Franklin et al., 2005; Leach et al., 2005), whereas the latter model considers that it is epigenetic and related to contact metasomatism (e.g., Einaudi and Burt, 1982; Meinert et al., 2005).

Recent mining exposures at the Yangla Cu deposit have made detailed investigation and research possible. In this paper, we present a detailed study of mineralogy and fluid inclusions from the deposit, combined with new geochronological (Re-Os dating using molybdenite) and isotopic data (sulfur isotopes in sulfides, carbon-oxygen isotopes in vein calcite and marble, and lead isotopes in whole rocks), to constrain its origin and hydrothermal evolution. These data provide a better insight into the ore-forming mechanisms at Yangla and clearly show the deposit to be an intrusion-related skarn.

Geologic Background

Tectonic framework of the Sanjiang metallogenetic domain

The Sanjiang metallogenetic domain in southwest China is located in the transitional area between the Tibetan Plateau and the South China block, and forms an important part of the Tethyan-Himalayan metallogenetic belt, with an area of about 1,000 km by 80 to 300 km wide (Fig. 1; Boulin, 1991; Mo et al., 1993; Yin and Harrison, 2000; Hou et al., 2007). The region is characterized by several NW-SE–trending ophiolite-decorated suture zones with regional-scale thrusts and adjacent magmatic belts, separating several microcontinental blocks (Fig. 1B; Zi et al., 2013). They record the opening and closure of the Tethys Ocean, including the Paleo-Tethys (Devonian-Triassic), Meso-Tethys (late Early Permian-Late Cretaceous), and Neo-Tethys (Late Triassic-Late Cretaceous), formed after the rift of the various microcontinental blocks from Gondwana (Metcalfe, 2006, 2013). Based on the ophiolitic sutures, four main branches for the Paleo-Tethys Ocean have been recognized in this area from northwest to southeast: the Garzê-Litang Ocean (suture I on Fig. 1), the Jinshajiang-Ailaoshan Ocean (sutures II and III on Fig. 1), the Longmu Tso-Shuanghu Ocean (suture IV_1), and the Changning-Menglian Ocean (suture IV_2 on Fig. 1; e.g., Mo et al., 1993; G. Pan et al., 2003; Xiao et al., 2008; Deng et al., 2014). The latter two oceans are considered to have been the main seaway, and are probably contiguous along strike with the Chiang Mai Ocean farther south in Thailand (Fig. 1A; Fan et al., 2010; J.-J. Zhu et al., 2011; Metcalfe, 2013; B.D. Wang et al., 2013). The Bangong-Nujiang suture (suture V on Fig. 1) in the west of the Sanjiang region was formed by closure of the Meso-Tethys Ocean (G. Pan et al., 2012). The Indus-Yarlung-Zangbo suture (suture VI on Fig. 1A) to the southwest represents a remnant of the Neo-Tethys Ocean (Metcalfe, 2006). Numerous igneous rocks and related ore deposits were generated since the Paleozoic, associated with the evolution of each stage of the Tethys Ocean (e.g., the Garzê-Litang belt, which includes the Pulang Cu and Gacun Ag polymetallic deposits; the Jinshajiang belt, which includes the Yangla Cu, Yulong Cu (Au-Mo), and Beiya Au (Cu) deposits; Lü et al., 1993; Mo et al., 1993; Hou et al., 2003, 2007; W.C. Li et al., 2011; Deng et al., 2014).

The Jinshajiang metallogenetic belt

The Jinshajiang suture is situated in the east of the Sanjiang region and probably connects with the Ailaoshan suture to the southeast, and also the Songma suture farther south in Vietnam (suture II_1 on Fig. 1A; X.F. Wang et al., 2000; Fan et al., 2010; Zi et al., 2012a, 2013; Metcalfe, 2013). The Jinshajiang metallogenetic belt trends northwest-southeast for over 1,000 km, and is composed of the Jinshajiang ophiolite-bearing suture zone and the flanking western Jomda-Weixi arc belt (arc belt VII on Fig. 1B), which is associated with the westward subduction of the Jinshajiang Paleo-Tethys Ocean (L.Q. Wang et al., 2002). It shares a border with the South China block to the east, including the Zhongza and Songpan-Garzê microcontinental block. West of the Jinshajiang and Ailaoshan sutures lie the Qamdo-Simao terrane and the Indochina block. These two blocks are bounded by the Changning-Menglian suture zone to the west, beyond which lie the West Qiangtang and Sibumasu blocks (Fig. 1; Metcalfe, 2006, 2013; Zi et al., 2012a).

The Qamdo-Simao terrane was possibly separated from the South China block during opening of the Jinshajiang Ocean in the Late Devonian or early Carboniferous (Mo et al., 1993; Zhong, 2000; Metcalfe, 2002; Hou et al., 2007; J.-J. Zhu et al., 2011). It is thought that the Eaqing Complex may be the metamorphic basement of this terrane, with an upper intercept zircon U-Pb age of 1627 ± 192 Ma (X.F. Wang et al., 2000). It occurs as fragments on both banks of the Jinshajiang River, mainly ~70 km north of the Yangla Cu deposit (it is too small to show at the scale of Fig. 1). Lower Ordovician low-grade metasedimentary rocks, including slates, phyllites, quartzites, and marbles, are the oldest rocks exposed in this area (apart from the basement), and are unconformably overlain by Middle Devonian to Permian shallow-marine sedimentary rocks (paralic and continental successions), followed by Lower-Middle Triassic carbonate-clastic rocks and Upper Triassic to Jurassic red-bed sedimentary rocks (G. Pan et al., 2003; Metcalfe, 2006; Zi et al., 2012a, 2013).

The Jinshajiang metallogenetic belt has undergone a complex evolution from the late Paleozoic to the Neogene, involving subduction of the Jinshajiang Ocean, arc-continent collision, postcollisional processes, and strike-slip motion (Zhan et al., 1998; Hou et al., 2007; Zi et al., 2013). A compilation of U-Pb ages for igneous rocks within the belt describes the tectonic history of the Jinshajiang Ocean. Pegmatoid cumulate gabbro from the ophiolite fragment has a U-Pb zircon age of 343.5 ± 2.7 Ma (Jian et al., 2009) and the Dongzhulin trondhjemite has been dated at 347 ± 7 Ma (zircon U-Pb; Zi et al., 2012a), indicating that the Jinshajiang Ocean probably opened in the early Carboniferous. Westward-directed subduction beneath the Qamdo-Simao terrane had begun by the Early Permian, with ages constrained by the subduction-related Jiyidu tonalite (285 ± 6 Ma, zircon U-Pb; Jian et al., 2008; Zi et al., 2012a). At the same time, a new ocean basin, the Garzê-Litang Ocean, opened to the east, rifting continental fragments including the Zhongza terrane from the South China block (Mo et al., 1993; G. Pan et al., 2003; Zi et al., 2013).

Following elimination of the Jinshajiang Ocean, crustal anatexis reflecting the earliest phases of collision produced high-silica rhyolites with Early Triassic ages (ca. 247–246 Ma; Zi et al., 2012b). Subsequently, the ophiolitic zone was unconformably overlain by Late Triassic molasse. The emplacement of high-K, calc-alkaline granitoids with ages from 234 to 214 Ma suggests that the Late Triassic was a period of early tectonic collapse and thermal relaxation in a postcollisional setting (Mo et al., 1993; J.-J. Zhu et al., 2011; Zi et al., 2013). The onset of India-Asia collision in the Cenozoic caused left-lateral movements of more than 500 km along the Ailao Shan-Red River strike-slip fault (Fig. 1; Zhong, 2000; Searle, 2006).

Two important pulses of intermediate to felsic intrusive activity and mineralization have been identified in this region (Mo et al., 2005; Hou et al., 2007). Triassic granitoids are represented by the Baimaxueshan (~248 Ma; Zi et al., 2012c), Ludian (234–214 Ma; Zi et al., 2012c), and Jiaren (~232 Ma) intrusions, which possibly formed after elimination of the Jinshajiang Ocean (Fig. 1B; J.-J. Zhu et al., 2011; Zi et al., 2012c, 2013). The Yangla Cu deposit is spatially related to the Jiaren intrusion. However, sparse mineralization also occurs in association with the other two intrusions.

A second pulse of intrusions was emplaced in the Eocene (~43–33 Ma) along the NW-SE–striking Jinshajiang fault system and Ailao Shan-Red River strike-slip fault (Fig. 1; L.L. Xu et al., 2012). These intrusions are associated with a number of porphyry-skarn Cu-Au (Mo) deposits, including the giant Yulong porphyry Cu (Au-Mo) belt in the north (Hou et al., 2003; Liang et al., 2009), and the Machangqing Cu-Mo (Hu et al., 1998), Yao'an Au (Bi et al., 2004), and Beiya Cu-Au (X.-W. Xu et al., 2007) deposits in the south (Fig. 1B; Hou et al., 2007; Y.-J. Lu et al., 2013). The Habo Au deposit occurs in the Ailaoshan Belt (35.5 ± 0.2 Ma at 2σ, Re-Os dating of molybdenite, X. Zhu et al., 2013). It is proposed that the regional strike-slip structural system may have controlled magma emplacement and ore formation (e.g., Hou et al., 2003).

Geology of the Yangla Cu Deposit

The Yangla Cu deposit is the largest Paleozoic deposit in the Jinshajiang metallogenic belt. The ore field is an N-S–trending linear area 25 km long × ~8 km wide, bounded by the Jinshajiang fault to the east and the Yangla fault to the west (Fig. 2; Zhan et al., 1998). The Jinshajiang fault is a regional-scale thrust, dipping 60° to 80° to the west (J. Pan, 1999), whereas the Yangla fault is only ~40 km long and N-S striking, with dips from 30° to 70° to the east. Previous exploration work has indicated there were seven mineralized centers dispersed from north to south within the area (Fig. 2; Zhan et al., 1998). However, only two of them are recognized to be economic at present; these are the Linong and Lunong ore zones, which

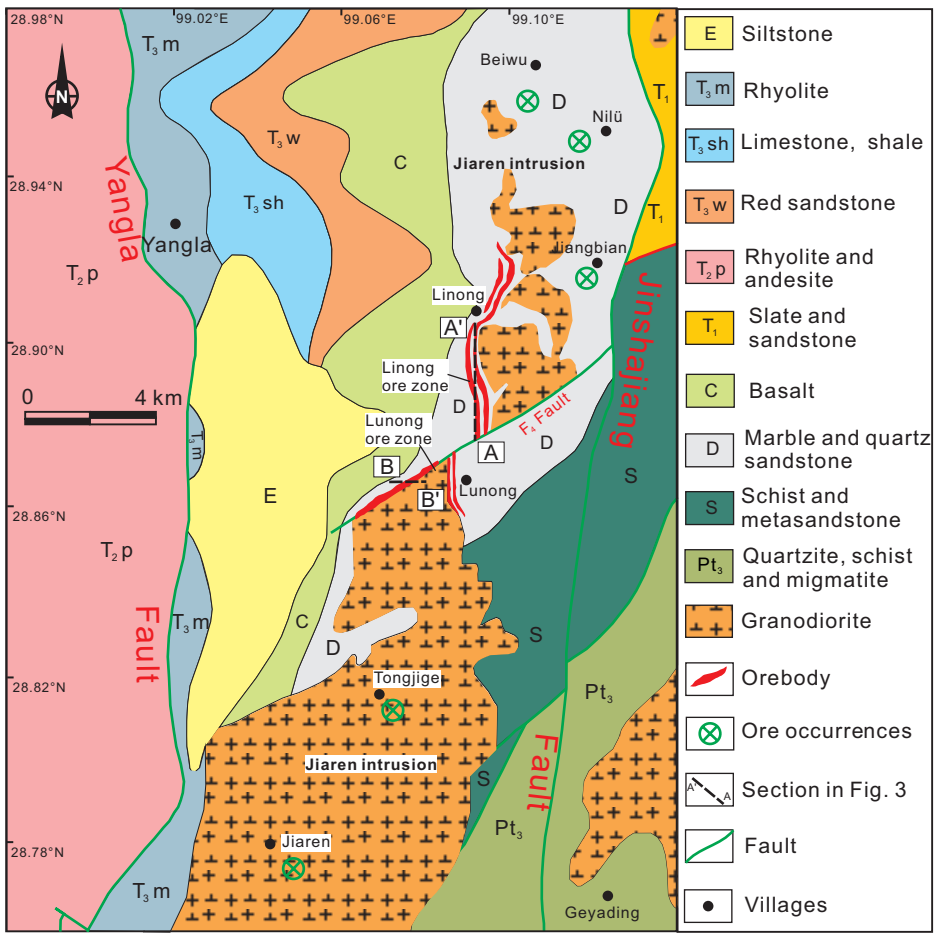

FIG. 2. Geologic map of the Yangla copper deposit and the distribution of orebodies (modified from J.-J. Zhu et al., 2011).

are separated by the NE-oriented F_4 normal fault (Zhan et al., 1998) in the middle part of the ore field (Fig. 2). The Linong ore zone accounts for 90% of the copper reserves in the district. This paper primarily focuses on these two ore zones.

Low-grade metamorphism is widespread in the ore field. Silurian schist and metasandstone are exposed in the southeast, in fault contact with Late Proterozoic metamorphic rocks and migmatite. The overlying Devonian sequences include the Jiangbian and Linong formations, which are composed of interbedded marble and quartz sandstone, with minor intercalated volcanic and siliceous rocks (Fig. 3). The top of the Jiangbian Formation and the middle to bottom part of the

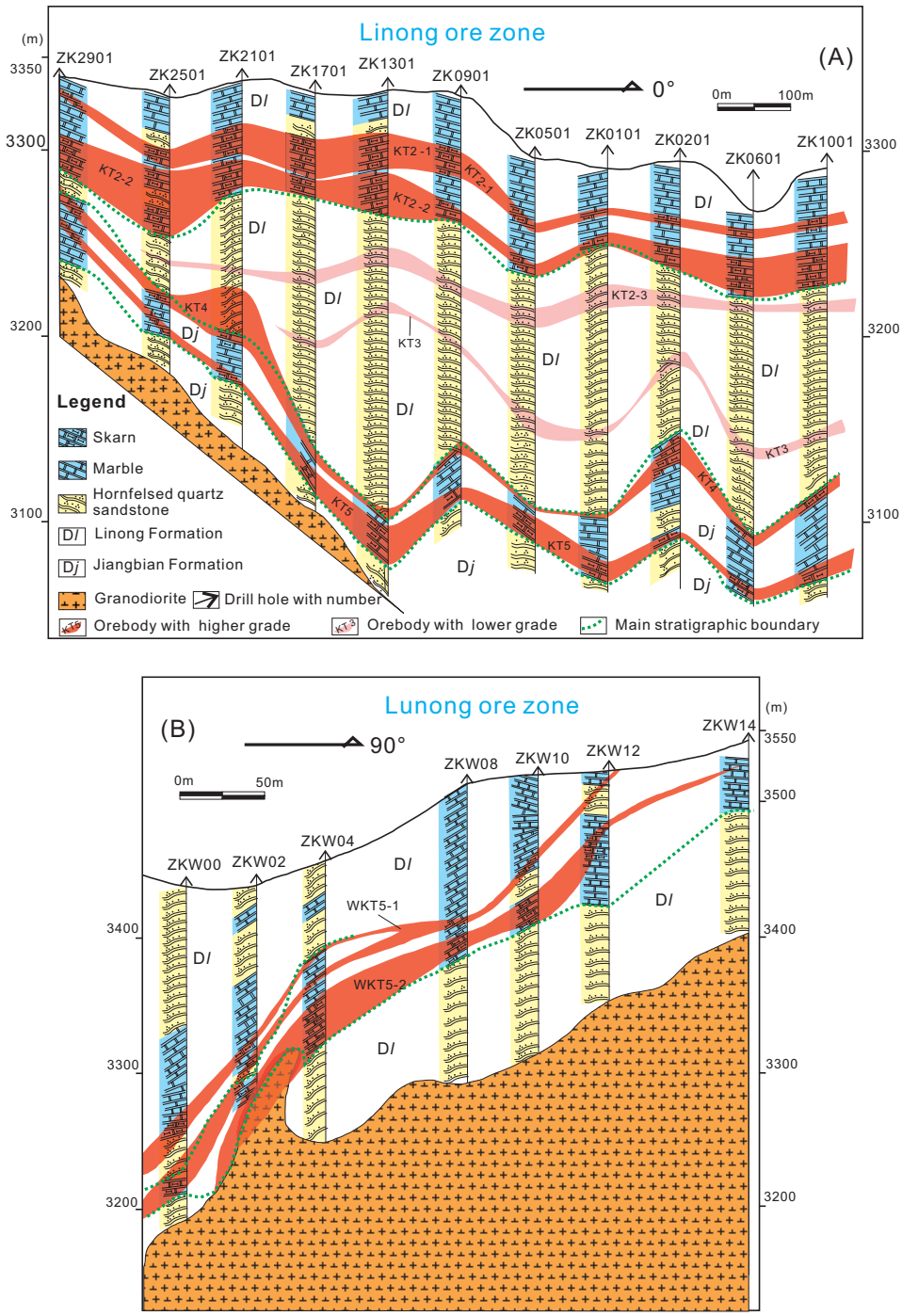

FIG. 3. Geologic cross sections through the Yangla Cu deposit, showing the spatial relationship among different strata units, intrusions, skarn, and orebodies (modified after Yunnan Copper (Group) Corporation, unpub. data, 2004). The connections of orebodies between different drill holes are based on mineral assemblages, ore textures, and strata correlations. The skarn orebodies are spatially associated with skarn-type alteration. (A) and (B) are for the Linong and Lunong ore zones, respectively. See Figure 2 for locations.

Linong Formation are the main hosts for mineralization; they dip 8° to 35° to the west-southwest and have a thickness of over 500 m. It has been suggested that fracture zones occur between different units of the Jiangbian and Linong formations (Gan et al., 1998; Zhan et al., 1998), but we were unable to confirm this in our study. Early Carboniferous basalt occurs to the west of the ore field and is unconformably overlain by Late Triassic sedimentary and volcanic sequences (Fig. 2).

The Jiaren batholithic complex intrudes the Silurian and Devonian quartz sandstone, with an outcrop area of ~150 km^2 (extending to the south beyond Fig. 2). The principal rock type is medium- to coarse-grained granodiorite, consisting of 35% to 40% plagioclase, 15% to 20% K-feldspar, 20% to 25% quartz, 10% to 15% hornblende, and minor amounts of biotite (~5%). Accessory minerals include zircon, titanite, apatite, and magnetite. Our previous studies (data below from J.-J. Zhu et al., 2011) reveal that the Jiaren intrusion was emplaced at ~232 Ma (233.1 ± 1.4 and 231.0 ± 1.6 Ma at 2σ, SIMS zircon U-Pb dating). These I-type granodiorite rocks are enriched in abundances of Si and large ion lithophile elements (LILEs, e.g., Rb, K, U; Rb = 73–152 μg/g), but depleted in high field strength elements (HFSEs, e.g., Nb, Ta, Ti, Y; Nb = 7.0–10.8 ppm, Y = 10.9–16.6 ppm). The systematic decrease in MgO, Fe_2O_3, TiO_2, and P_2O_5 with SiO_2 contents suggests significant fractionation involving hornblende, Fe-Ti oxides (e.g., ilmenite), and apatite. Hornblende and titanite stabilities might reflect relatively high water concentrations (Naney, 1983; Ridolfi et al., 2010) and high magmatic oxidation states (Foley and Wheller, 1990), respectively. In addition, they have high initial $^{87}Sr/^{86}Sr$ ratios (0.7078–0.7148), negative $\varepsilon_{Nd}(t)$ values (–5.1 to –6.7), and variable $\varepsilon_{Hf}(t)$ values (–8.6 to +2.8). Taken together, it is suggested that the Jiaren intrusion has a mixed mantle-crust origin (J.-J. Zhu et al., 2011).

Alteration and mineralization

Wall-rock alteration is extensive and intensive in the mining area, and consists of skarn, silica, carbonate, and supergene alteration. Skarn-type alteration mainly occurs in the exocontact zone between the granodioritic intrusions and the Devonian strata, producing calc-silicates including prograde and retrograde skarn. Prograde skarn (anhydrous skarn) is mainly composed of garnet, diopside, and hedenbergite. Retrograde skarn (hydrous skarn) consists of a mixture of sericite, actinolite, grunerite, epidote, and chlorite, developed as alteration products of early-stage skarn minerals. The skarn zones show stratigraphic control and typically occur between the marble and quartz sandstone. They form several nearly horizontal to sloping sheets, within ~20 to 250 m of the main intrusive contact (Fig. 3A). Minor skarn alteration can also be found along the contact zone between the intrusions and the Devonian marble in the Lunong ore zone (Fig. 3B). The quartz sandstone sequences were generally hornfelsed, with skarn alteration characterized by small amounts of garnet veining or chloritization (Fig. 4A).

Silica and carbonate alteration generally overprint the earlier skarn and consist of quartz and calcite with minor amounts of siderite, respectively. Because the two kinds of alteration typically coexist with the prograde and retrograde skarn alteration, they also mainly occur between the marble and quartz sandstone sequences. Minor silica and carbonate alteration are also characterized by pyrite- and chalcopyrite-bearing quartz and calcite veinlets that cut or follow the bedding of the hornfelsed quartz sandstone nearby the skarn zones (Fig. 4A, B).

The Yangla deposit contains weathered zones with a supergene alteration mineral assemblage of malachite, limonite, and azurite. Supergene effects are mainly centered near the surface (0–50 m underground) of the Lunong ore zone.

Compared with the country rocks, the granitic intrusions are generally fresh with little hydrothermal alteration. However, the Jiaren granodiorite in the Lunong ore zone locally displays skarn-type alteration (endoskarn) where it is in contact with the marble (Fig. 3B).

Copper mineralization is spatially associated with skarn-type alteration zones (~80%; Yangla mine staff, pers. com., 2011) and, to a lesser extent, with the adjacent hornfelsed quartz sandstone sequences (~20%). The Linong ore zone contains eight economic orebodies, individually consisting of variable amounts of skarn and hornfelsed quartz sandstone ores (Fig. 3A). Most of the ore zones are located between different units of the Jiangbian and Linong formations and generally show stratigraphic control and stratiform-like shapes (similar to "mantos" proposed by Meinert, 1982; Fig. 3A), but the contacts between orebodies and marbles are typically irregular and discordant (Fig. 4D). These individual orebodies range between 0.7 and 44 m in thickness and from 680 to 2,200 m in length, and generally dip 5° to 45° to the northwest (Fig. 3A; Table 1). The main orebodies (KT2-1, KT2-2, KT4, and KT5) contain an average of 1.03% copper in mainly skarn ores. They typically have metasomatic contacts with marble, which occurs locally as enclaves in the skarn ores (Fig. 4C, D). Near the skarn contacts, marble contains veinlets of sulfides and minor skarn patches (Fig. 4D). The other four orebodies consist of hornfelsed quartz sandstone ores, with a lower copper grade of 0.76% to 0.97% (Table 1). Some skarn minerals can also be found in these ores. Chalcopyrite is the most important Cu-bearing mineral in the Linong ore zone, occurring as massive or disseminated subhedral grains with other sulfides in skarn ores and in veins with quartz or calcite cutting stratifications in hornfelsed quartz sandstone ores.

The Lunong ore zone contains four economic orebodies, with average grades in excess of 1.2% Cu (Table 1). Because of supergene alteration, most of the orebodies are oxidized, characterized by the occurrence of a large amount of secondary malachite and azurite. They also have a large range in length (250–804 m) and thickness (1.1–52 m). Two of the orebodies (WKT5-1 and WKT5-2; Fig. 3B) have an NW-NNW trend and dip between 31° and 76°, and are located to the northwest of the Jiaren intrusion (Table 1; Figs. 2, 3B). The other two orebodies (WKT1 and WKT4) are located to the northeast of the intrusion, and dip from 45° to 87° to the west (Table 1; Fig. 2). Compared to the Linong ore zone, the orebodies in the Lunong zone occur not only between different stratigraphic units, but also along the contact zones between the Jiaren intrusion and marble of the Linong Formation. Here, the mineralization is characterized by strata-bound and minor lenticular skarn and hornfelsed quartz sandstone ores (Fig. 3B). Small amounts of endoskarn mineralization are also recognized within the margin of the granodiorite.

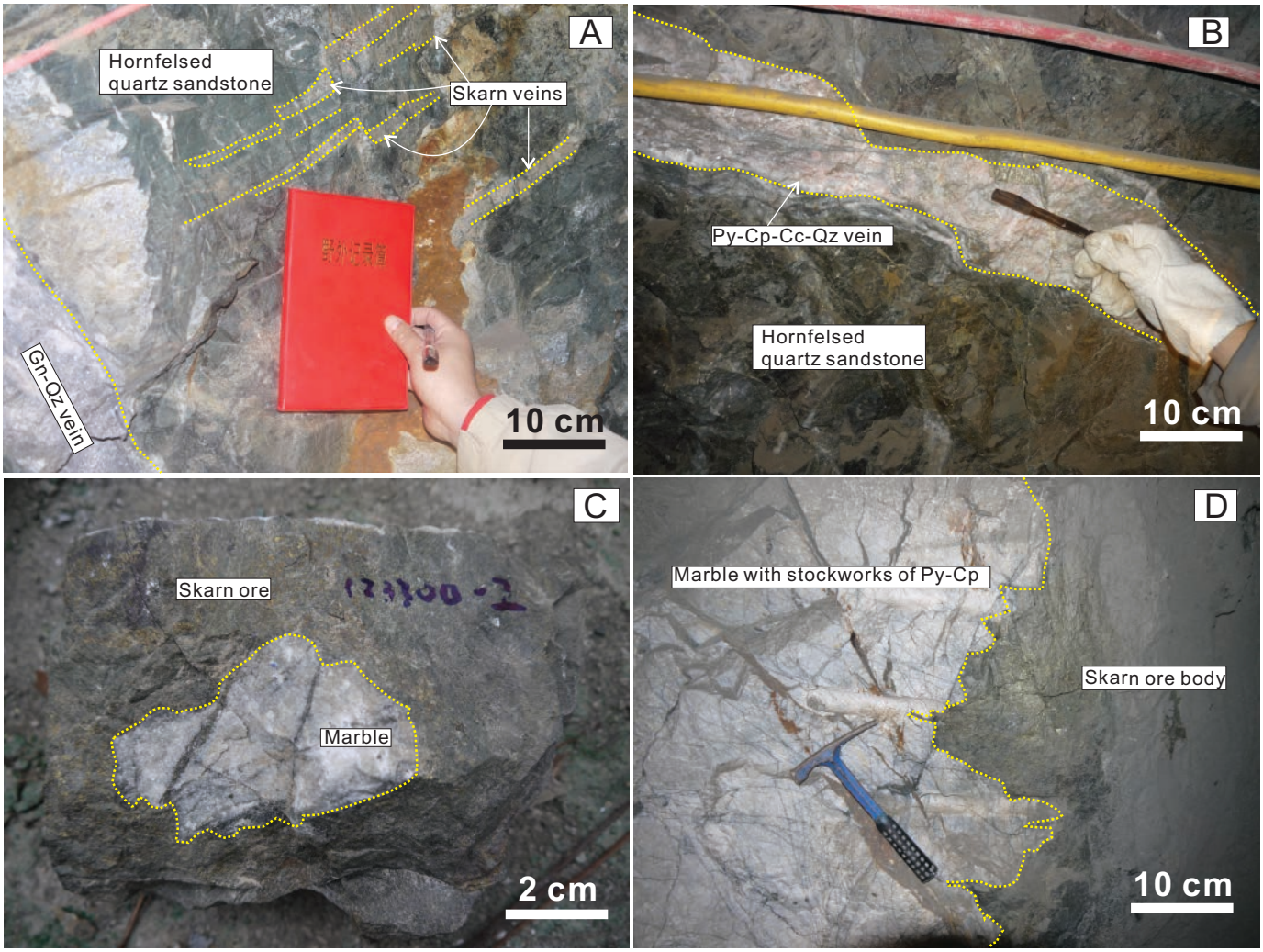

FIG. 4. Photographs showing (A) skarn alteration in the hornfelsed quartz sandstone characterized by minor garnet veinlets; (B) sulfide-bearing quartz and calcite veinlets cutting or along the bedding of the hornfelsed quartz sandstone; (C) marble fragment as an enclave in the skarn ore; some skarn veinlets crosscut the marble; and (D) skarn ore in irregular and transgressive contact with marble.

TABLE 1. A Summary of the Geometrical Features and Metal Contents of Major Orebodies in the Yangla Deposit[1]

Orebody no.	Tendency	Dip	Length (m)	Thickness (m)	Average Cu (wt %)	Ore (million tonnes)	Ore type
Linong ore zone							
KT2–1	NNW	12°–40°	1,100	9–44	1.03	15.2	Skarn and minor HM
KT2–2	NW	12°–35°	2,200	11–41	1.02	19.1	
KT2–3	NNW-W	10°–38°	1,300	0.7–25	0.83	3.2	HM
KT2–7	NNW	15°–40°	900	1.5–19	0.97	1.1	
KT3	NW	15°–45°	900	1.7–18	0.76	1.2	
KT4–1	NW	10°–25°	680	0.9–35	0.88	1.2	
KT4	NW	5°–30°	1,200	1–22	1.47	5.3	Skarn and HM
KT5	NW	8°–18°	1,900	1.1–29	0.98	12.8	Skarn and minor HM
Lunong ore zone							
WKT1	W	50°–87°	250	1.4–19	1.03	–	Skarn
WKT4	W-NW	45°–78°	804	1.1–21	1.77	–	Skarn and HM
WKT5–1	NW-NNW	31°–70°	682	1.2–52	1.18	–	
WKT5–2	NW-NNW	37°–76°	343	1.1–31	1.15	–	

Abbreviations: HM = hornfelsed quartz sandstone; – = no data
[1] Yunnan Copper (Group) Corporation, 2004, unpub. data

Samples and Analytical Methods

The Linong and Lunong ore zones share similar characteristics, but the Linong ore zone is less oxidized; consequently, most of the samples for this study were collected from that part of the deposit. Representative samples of the orebodies were mainly collected from underground workings at different levels (i.e., at the 3,050, 3,075, 3,175, 3,200, 3,250, and 3,275 levels, Fig. 3), and a few samples were collected from surface outcrops.

Mineral chemistry analysis

Compositions of skarn minerals (garnet, diopside, and hedenbergite) were obtained on an EPMA-1600 electron probe microanalyzer (EPMA) at the State Key Laboratory of Ore Deposit Geochemistry, Institute of Geochemistry, Chinese Academy of Sciences, using natural minerals for standards. Standard operating conditions used were an accelerating voltage of 25 kV and a beam current of 10 nA, with a beam size of 1-μm diameter. Some additional energy-dispersive analyses and backscattered electron images were obtained at the University of Alberta, using a JEOL 8900 EPMA with an accelerating voltage of 15 kV and a beam current of 20 nA.

Re-Os isotope dating

Six molybdenite samples intergrown with chalcopyrite from the 3,075 level of the Linong ore zone were handpicked under the binocular microscope after crushing to get >99% purity mineral separate. The separates were then ground to pass 200 mesh and blended to assure homogeneity.

Re-Os isotope analysis was performed on a TJA X-series inductively coupled plasma-mass spectrometer (ICP-MS) at the National Research Center of Geoanalysis, Chinese Academy of Geological Sciences, in Beijing. Powdered molybdenite was weighed and transferred to a Carius tube for dissolution. Enriched ^{190}Os and enriched ^{185}Re were used as spikes to correct for common Os and mass fractionation. Osmium was separated using in situ distillation equipment and Re was then isolated by anion exchange column. The detailed procedures are described by Du et al. (2004). Procedural blanks are 0.0253 ± 0.0005 ng for Re and negligible for ^{187}Os. The ^{187}Re decay constant of 1.666×10^{-11} year^{-1} was used to calculate the molybdenite model ages (Smoliar et al., 1996). Absolute uncertainties (2σ) include propagation of uncertainties in Re and Os mass spectrometer measurements, abundances and isotopic compositions of the blank, and spike calibrations. The measured model age of standard (GBW04435) is 140.1 ± 2.0 Ma (2σ), which is consistent with the certified value (139.6 ± 3.8 Ma; Du et al., 2004). The Re-Os isotope data were calculated and plotted using the ISOPLOT software of Ludwig (2008).

Stable isotope analysis

Sulfide and calcite grains were carefully handpicked under a binocular microscope after crushing and cleaning. The purity of single mineral separates was over 99%.

Sulfur isotope analyses of sulfide minerals including pyrite, chalcopyrite, pyrrhotite, and molybdenite were carried out at the State Key Laboratory of Environmental Geochemistry, Institute of Geochemistry, Chinese Academy of Sciences. Sulfur was extracted with a continuous-flow device, wherein 0.1 to 0.3 mg of sulfide was converted to SO_2 in an EA-IsoPrime isotope ratio mass spectrometer (Euro3000, GV Instruments). Data are reported using the delta notation in ‰ relative to the Cañon Diablo Troilite (CDT). The acanthite samples GBW04414 (Ag_2S, state reference material of China) were used as external standards. Its measured δ^{34}S value is –0.11 ± 0.11‰ (n = 11; the recommended value is –0.07 ± 0.13‰; Ding et al., 2001), and precision of unknown analyses is estimated to be ±0.2‰ (2σ).

Lead isotope compositions of wall rocks including basalts were obtained using a Finnigan Triton multicollector mass spectrometer at the China University of Geosciences, Wuhan. Pb was separated by a conventional AG50 1 × 8 anion exchange technique. The measured ^{206}Pb/^{204}Pb, ^{207}Pb/^{204}Pb, and ^{208}Pb /^{204}Pb ratios of the NBS981 Pb standard were 16.932 (the recommended value is 16.9356), 15.485 (the recommended value is 15.4891), and 36.685 (the recommended value is 36.7006; Todt et al., 1996), respectively. Detailed analytical procedures are described by Liu et al. (2001).

Carbon and oxygen isotope compositions of calcite and marble were determined on a Finnigan MAT-253 mass spectrometer at the State Key Laboratory of Environmental Geochemistry, Institute of Geochemistry, Chinese Academy of Sciences. CO_2 gas was extracted by reaction with pure phosphoric acid in a thermostatic bath for 24 h. Carbon and oxygen isotope ratios are expressed in the conventional delta notation and given in ‰ values relative to Pee Dee Belemnite (PDB) for carbon (Coplen et al., 1983) and Vienna-Standard Mean Ocean Water (V-SMOW) for oxygen. The analytical precision (2σ) is ±0.2‰ for δ^{13}C and ±2‰ for δ^{18}O.

Fluid inclusion microthermometry

Fluid inclusion analysis was undertaken at the University of Alberta. A set of eight Cu-bearing samples was collected, including two andradite-diopside skarn ores and six quartz-calcite veins. Doubly polished thin sections (~100 μm thick) were prepared and selected chips were analyzed using a Linkham THMSG600 microthermometric stage. The stage was calibrated using a set of synthetic fluid inclusion standards from Syn Flinc, with a precision of ±0.1°C near or below 0°C and ±1°C at higher temperatures. Fluid inclusions were cooled to –150°C and then heated progressively until total homogenization, measuring all observed phase changes. Sequential freezing was usually required to obtain accurate ice-melting temperatures (Haynes, 1985). Heating/cooling rates were restricted to <20°C/min, and 1° to 0.1°C/min near phase transformations.

The equation of Hall et al. (1988) was used to calculate salinities of liquid-rich fluid inclusions from measured ice-melting temperatures, whereas salinities of hypersaline inclusions were calculated from measured halite-melting temperatures using the equation of Sterner et al. (1988).

Skarn Mineralogy and Paragenesis

Based on detailed field investigations and observed cross-cutting relationships, three stages of skarn formation and ore deposition have been recognized (pre-ore, main ore, and late ore), with a fourth supergene oxidation stage. The paragenesis is illustrated in Figure 5.

FIG. 5. Mineral paragenesis for the Yangla Cu deposit.

Pre-ore stage

Anhydrous minerals including garnet and pyroxene associated with prograde skarn alteration represent the earliest stage of skarn formation. No sulfides were present in this stage.

Garnets occur widely in the skarn zone as fine- to coarse-grained (up to 5 mm) euhedral to subhedral crystals, commonly intergrown with pyroxenes (Fig. 6A), or independently without other calc-silicate minerals (Fig. 6D). Electron microprobe analyses (Table 2) indicate that garnets in the Yangla Cu deposit are mainly andraditic (Ad_{83} to pure andradite; Fig. 7). The average composition is Ad_{96} $Gr_{2\sim3}Py_{0\sim1}$ (based on 26 EPMA analyses). Individual garnet crystals have relatively homogeneous compositions, with insignificant zoning. Most

TABLE 2. Representative Electron Microprobe Analyses of Garnet and Clinopyroxene (wt %) from the Yangla Cu Deposit

	Garnet						Clinopyroxene				
	1	2	3	4	5		1	2	3	4	5
SiO_2	35.32	34.98	41.89	36.87	37.75		54.09	54.22	53.37	47.66	48.57
TiO_2	0.00	0.00	0.01	0.00	0.37		0.01	0.04	0.01	0.08	0.03
Al_2O_3	0.26	0.33	0.13	1.52	2.35		0.01	0.06	0.01	0.32	0.19
Cr_2O_3	0.00	0.00	0.12	0.00	0.01		0.01	0.00	0.00	0.06	0.00
FeO	28.69	28.45	38.13	27.51	26.48		2.37	3.47	5.05	27.89	24.86
MnO	0.26	0.17	0.67	0.16	0.37		0.22	0.24	0.20	0.55	0.60
MgO	0.00	0.00	4.36	0.01	0.05		16.54	16.41	14.90	1.29	2.50
CaO	34.05	34.23	12.90	32.60	31.01		26.72	26.26	26.03	22.78	23.28
Na_2O	-	-	-	-	-		0.02	0.03	0.03	0.05	0.06
Total	98.58	98.16	98.20	98.67	98.39		100.00	100.71	99.60	100.67	100.08
Adr	98.7	98.4	94.0	91.6	83.9	Di	97.7	94.6	88.0	8.4	16.0
Gr	1.3	1.6	1.5	7.8	13.6	Jo	0.6	0.6	0.5	1.6	1.8
Pyr	0.0	0.0	3.5	0.6	2.5	Hd	1.7	4.7	11.5	90.0	82.2

Abbreviations: Ad = andradite, Di = diopside, Gr = grossular, Hd = hedenbergite, Jo = johannsenite, Pyr = pyralspite (pyrope + almandine + spessartine)

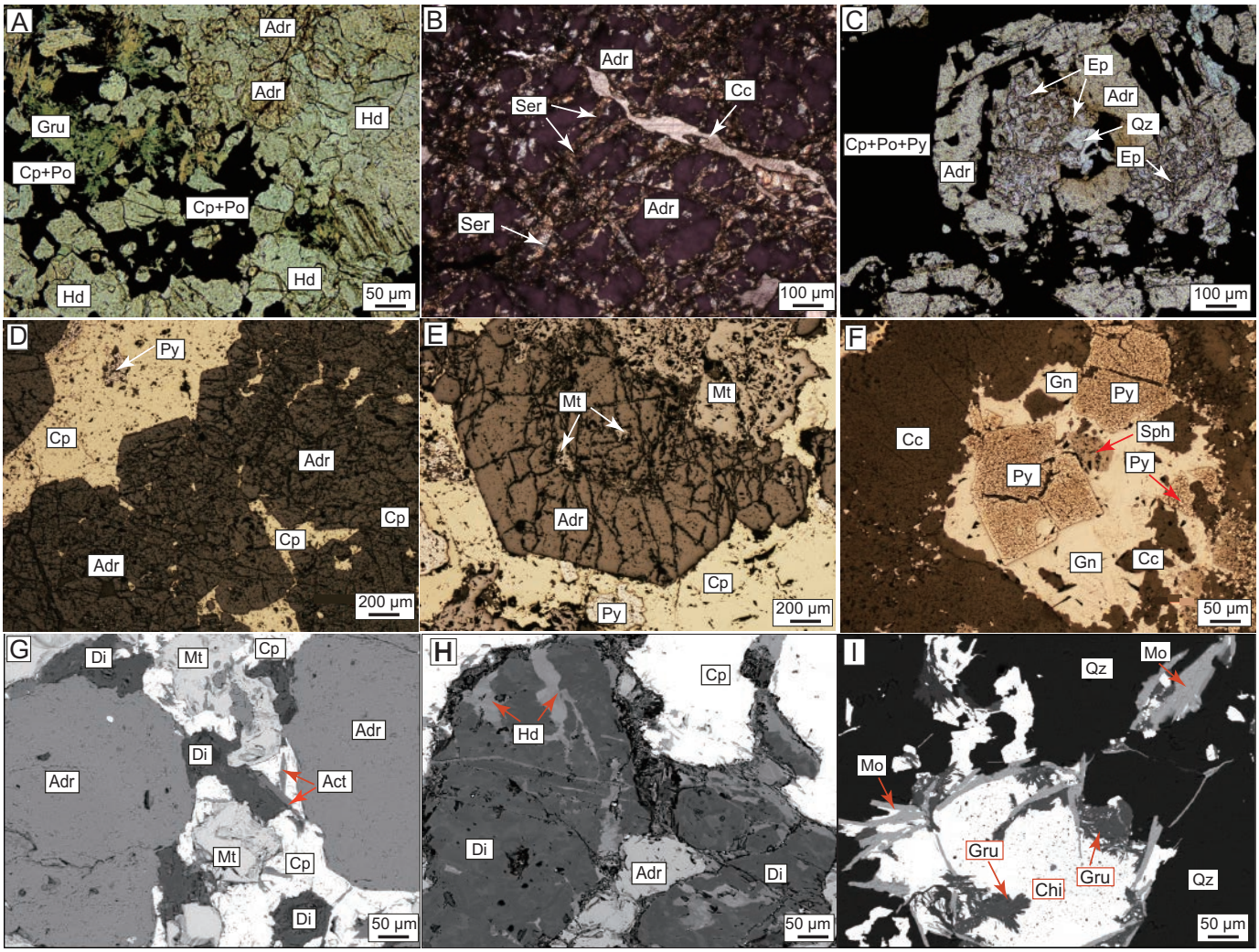

FIG. 6. Representative transmitted (A-C) and reflected light (D-F) photomicrographs and backscattered electron images (G-I) showing mineral assemblages and textural features from the Yangla Cu deposit. (A) Andradite and hedenbergite are overprinted by Fe-Cu sulfides and hydrous minerals such as grunerite; plane-polarized light. (B) Sericite veinlets crosscutting andradite, which are themselves cut by late-stage calcite veinlets; cross-polarized light. (C) Core of an andradite crystal replaced by epidote grains and quartz, plus interstitial Cu-Fe sulfides; plane-polarized light. (D) Euhedral andradite with interstitial chalcopyrite. (E) Subhedral andradite with interstitial magnetite, overprinted by pyrite and chalcopyrite. (F) Subhedral pyrite enclosed by galena, which is intergrowth with calcite and sphalerite. (G) Magnetite and chalcopyrite fill the interstices between andradite and diopside, which are replaced by acicular actinolite. (H) Hedenbergite veinlets crosscutting earlier diopside. (I) Coexisting quartz, molybdenite, grunerite, and chiviatite. Abbreviations: adr = andradite, cc = calcite, chi = chiviatite, cp = chalcopyrite, di = diopside, ep = epidote, gru = grunerite, hd = hedenbergite, mo = molybdenite, mt = magnetite, po = pyrrhotite, py = pyrite, qz = quartz.

of these garnets are partially altered to grunerite, sericite, and epidote (Fig. 6A-C).

Pyroxenes are generally pale green to dark green in color. They occur as fine- to medium-grained (1–3 mm) anhedral to subhedral crystals, and are generally associated with garnet (Fig. 6A, G, H). Two types of pyroxene are recognized by EPMA: diopside (average composition: Hd_6Di_{94}) and hedenbergite (average composition: $Hd_{86}Di_{13}Jo_1$; Fig. 7). Figure 6H shows that veinlets of hedenbergite crosscut earlier diopside, implying a trend of increasing Fe content in the hydrothermal fluid, which has also been observed in other skarn deposits (e.g., Chang and Meinert, 2008; Shu et al., 2013).

Overall, garnets in the Yangla Cu deposit display compositions similar to those from other skarn Cu deposits (Fig. 7; Meinert, 1992; Meinert et al., 1997; Calagari and Hosseinzadeh, 2006). However, pyroxene compositions are more Fe rich (hedenbergitic) than in other Cu-bearing skarns around the world (which tend to be more magnesium rich; Fig. 7). Mn/Fe ratios in pyroxenes typically vary from 0.01 to 0.08, which is typical for pyroxenes from skarn Cu deposits worldwide (Mn/Fe < 0.1, Fig. 7; Nakano et al., 1994).

Main ore stage

The main ore stage is characterized by the occurrence of an assemblage of hydrous silicate minerals, Fe oxides, Cu-Fe-Mo-Bi sulfides, and quartz, associated with retrograde skarn alteration and silicification. Retrograde skarn minerals include sericite, epidote, chlorite, and amphibole, which overprint

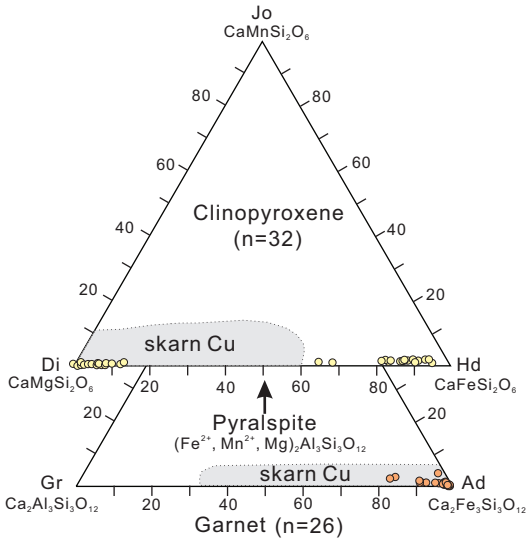

FIG. 7. Ternary diagrams summarizing garnet and clinopyroxene compositions in the Yangla Cu deposit. Shaded areas indicate clinopyroxene and garnet compositional ranges for Cu skarn deposits summarized by Meinert (1992). Abbreviations: ad = andradite, di = diopside, gr = grossular, hd = hedenbergite, jo = johannsenite, pyralspite = (pyrope + almandine + spessartine).

prograde garnet and pyroxene (Fig. 6A-C, G, I). Amphiboles occur as grunerite and actinolite, with minor tremolite, and form radiating or acicular aggregates (Fig. 6A, G, I). Iron-rich amphiboles are characteristic of Cu-bearing skarns (Meinert et al., 2005). Magnetite is abundant and typically fills fractures in garnets (Fig. 6E).

Primary Cu mineralization consists mostly of chalcopyrite and minor bornite. These sulfides occur as disseminations or as veinlets in the skarn. Together with Fe sulfides (i.e., pyrite and pyrrhotite) and quartz, Cu-Fe sulfides typically fill the interstices between garnets or cut the skarn as veins (Fig. 6A-E, G, H). Some chalcopyrite veins also cut magnetite, indicating that the Cu mineralization occurred later than the deposition of magnetite. Islands of pyrite in the chalcopyrite are also common (Fig. 6D, E). Most of the Fe-Cu sulfides in the main ore stage are anhedral with fine to coarse grains. Minor molybdenite occurs mainly with quartz, grunerite, and chalcopyrite, locally with chiviatite (Fig. 6I) and bismuthinite.

Some Cu mineralization also occurs in the hornfelsed quartz sandstone, cutting the stratification as chalcopyrite + pyrite + chlorite veinlets.

Late ore stage

Carbonate and silica alteration characterize the late ore stage, with deposition of calcite and quartz, plus minor chalcopyrite, pyrite, galena, sphalerite, and siderite (Fig. 6F).

Based on observed crosscutting relationships, calcite in the late ore stage appears to have formed in two substages (Fig. 5): an early substage of calcite in fractures cutting minerals from the pre-ore stage (e.g., sericite and andradite, Fig. 6B) and filling interstices between diopside crystals, and a late substage of large calcite veins (~10 cm wide, ~20 m long) cutting hornfelsed quartz sandstone ± skarns (Fig. 4A, B).

Pyrite in the early substage usually occurs as medium- to coarse-grained (up to 5 mm) subhedral-euhedral crystals, crosscut or overgrown by galena and sphalerite (Fig. 6F).

Supergene stage

The supergene stage is characterized by the formation of secondary Cu minerals such as malachite and azurite, which replace primary chalcopyrite and bornite. Together with limonite, these supergene minerals occur mainly near the surface (0–50 m underground) in the Lunong ore zone. Minor amounts of secondary minerals also occur along veins or fracture coatings at depth (200–300 m underground) in the skarn.

Re-Os Isotope Dating

The Re-Os data for six molybdenite samples are presented in Table 3. Rhenium contents range from 15.2 to 155.0 ppm and common Os ranges from 0.026 to 1.929 ppb. Calculated model ages are all within error of each other, ranging from 230.9 ± 3.3 (2σ) to 232.9 ± 3.3 Ma (2σ). These results yielded a well-constrained ^{187}Re-^{187}Os isochron age of 232.0 ± 1.5 Ma (2σ, MSWD = 0.48) and a weighted average age of 231.8 ± 1.3 Ma (95% confidence level with MSWD = 0.26; Fig. 8). This age is in good agreement with the age of the granitoids in the Yangla Cu deposit (233.1 ± 1.4 and 231.0 ± 1.6 Ma at 2σ; J.-J. Zhu et al., 2011). The zero isochron intercept indicates that there is no detectable common Os in the molybdenite samples, as is observed in other ore deposits around the world (e.g., Luck and Allègre, 1982; Drobe et al., 2013).

Stable Isotope Studies

Sulfur isotopes

Thirty-one samples were collected for sulfur isotope analysis: 23 from the Linong ore zone, and eight from the Lunong ore zone (Fig. 9; Table 4). For the Linong ore zone, 15 pyrite samples have δ^{34}S values between –0.9 and 2.6‰ (average =

TABLE 3. Re-Os Isotope Analyses for Molybdenite from the Yangla Cu Deposit

Sample no.	Weight (g)	Re (μg/g)	Initial Os ± 2σ (ng/g)	^{187}Re ± 2σ (μg/g)	^{187}Os ± 2σ (ng/g)	Age (Ma) ± 2σ
091201-1	0.020	152.9 ± 1.2	0.0026 ± 0.124	96.1 ± 0.8	370.4 ± 3.1	230.9 ± 3.3
091201-2	0.020	115.7 ± 0.9	0.2527 ± 0.043	72.7 ± 0.6	281.7 ± 2.4	232.1 ± 3.3
091201-3	0.021	15.2 ± 0.1	0.0026 ± 0.124	9.6 ± 0.1	36.9 ± 0.3	230.9 ± 3.3
091201-4	0.020	143.4 ± 1.1	0.1219 ± 0.084	90.1 ± 0.6	350.5 ± 0.3	232.9 ± 3.3
091201-5	0.020	18.2 ± 0.2	0.0027 ± 0.168	11.5 ± 0.1	44.5 ± 0.4	232.7 ± 3.5
100104-6	0.010	155.0 ± 1.1	0.1929 ± 0.067	97.4 ± 0.7	376.9 ± 3.3	231.7 ± 3.3

Note: Age calculations use ^{187}Re decay constant of 1.666 × 10^{-11} yr^{-1} (Smoliar et al., 1996)

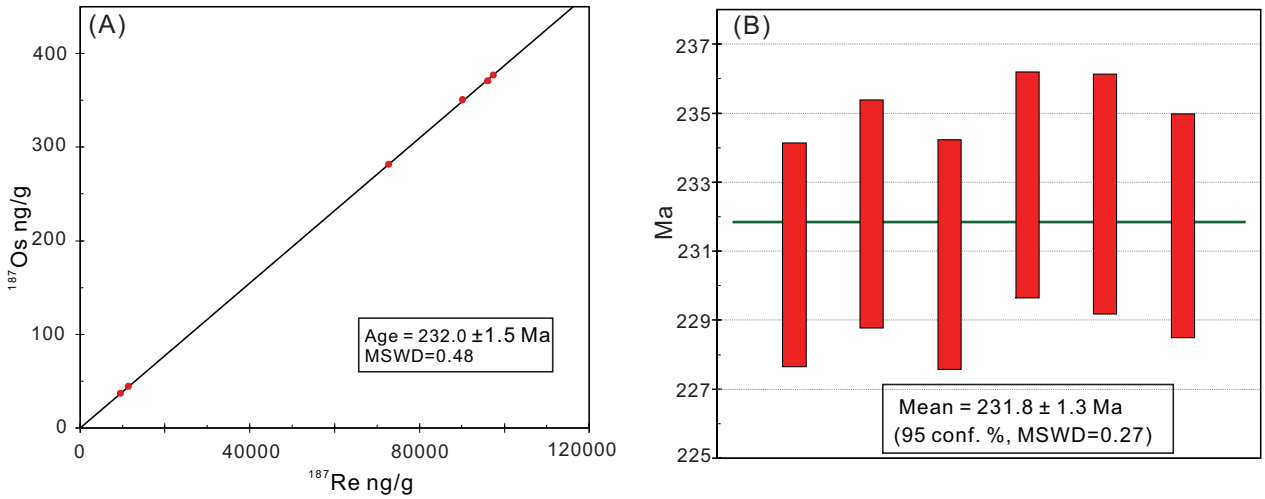

FIG. 8. Molybdenite Re-Os isotope analyses for the Yangla Cu deposit. (A) Isochron age of molybdenite. (B) Weighted average Re-Os model age of seven analyses. MSWD = mean squared weighted deviates, a measure of scatter.

1.34 ± 1.0, n = 15), whereas six molybdenite samples have a narrow range from 0.6 to 0.9‰ (average = 0.7 ± 0.1, n = 6). One chalcopyrite sample has a δ^{34}S value of 1.8‰, and one pyrrhotite sample has a value of –0.8‰.

Eight sulfide samples (four pyrrhotite, one pyrite, and three chalcopyrite) from the Lunong ore zone have a uniform range of δ^{34}S values from –1.9 to –1.7‰ (average = –1.8 ± 0.1‰, n = 8; Table 4, Fig. 9). One diagenetic pyrite sample from Carboniferous basalt in the Yangla mining area has a δ^{34}S value of –32.5‰ (Zhan et al., 1998), significantly lower than the data above.

The δ^{34}S values of the coexisting fluids ($\delta^{34}S_{\Sigma S}$) are related to temperature, pH, and f_{O_2} during sulfide precipitation (Ohmoto and Rye, 1979). The Yangla Cu deposit has an assemblage of pyrite, pyrrhotite, and magnetite but lacks sulfates. This indicates relatively low f_{O_2} conditions (Ohmoto, 1972) and suggests that the fluids were dominated by H_2S; consequently, the δ^{34}S values of the sulfide minerals likely closely reflect the bulk fluid values (Ohmoto and Rye, 1979). Of the minerals analyzed, chalcopyrite has the lowest temperature-dependent fractionation relative to H_2S, and so provides the best estimate for the bulk fluid S isotope composition: ~+1.8‰ for the Linong ore zone, and ~–1.8‰ for Lunong.

Lead isotopes

Lead isotope data for basalt, wall-rock, and granodiorite samples are listed in Table 5. Eight basalt samples have present-day whole-rock Pb isotope ratios of $^{206}Pb/^{204}Pb$ = 18.282

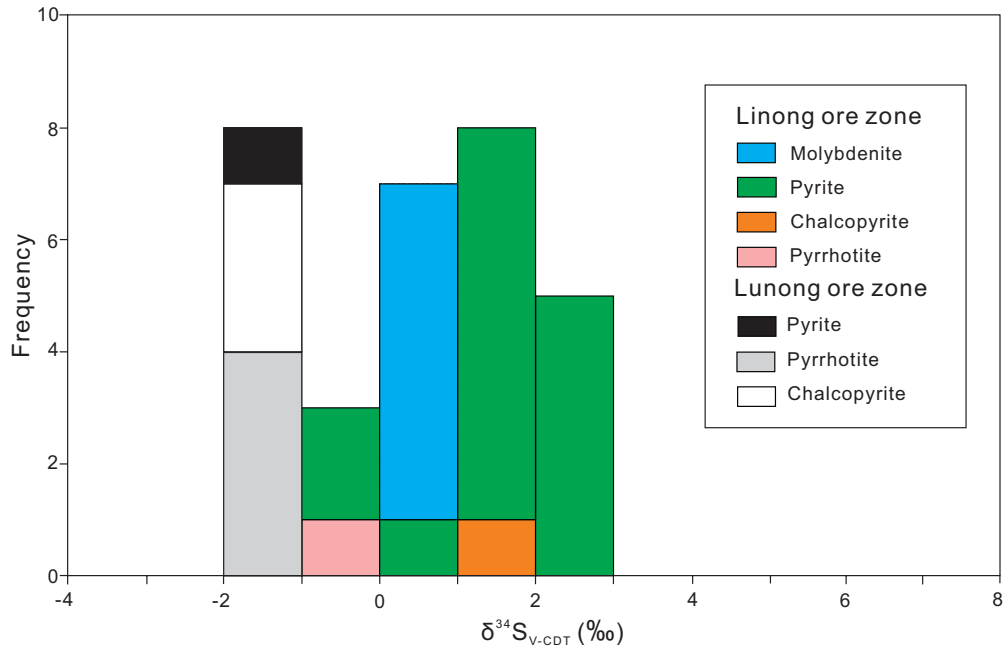

FIG. 9. Frequency histogram of δ^{34}S values for sulfide minerals from the Yangla Cu deposit.

TABLE 4. Sulfur Isotope Data for Sulfide Minerals from the Yangla Deposit

Sample no.	Ore zones	Ore type	Mineral	$\delta^{34}S_{V\text{-}CDT}$‰
083250-60	Linong	Skarn	Pyrrhotite	–0.8
093200-24			Chalcopyrite	1.8
083250-12			Pyrite	1.2
093200-17				2.1
103200-2-2		Hornfelsed quartz metasandstone	Pyrite	–0.8
103200-2-1				–0.9
093200-23				2.6
083250-13			Pyrite	1.3
093200-7				1.5
093175-1-1		Skarn	Pyrite	0.4
093200-5				1.8
093200-8				1.6
093200-4				2.2
093200-6				1.8
093200-9				2.2
093200-9-0				2
103175-1				1.2
083075-3			Molybdenite	0.6
083075-4				0.7
083075-5				0.9
083075-6				0.6
083075-7				0.7
083075-8				0.8
LuN-5	Lunong	Skarn	Pyrrhotite	–1.9
LuN-8				–1.9
LuN-6				–1.9
LuN-7				–1.8
LuN-9			Pyrite	–1.8
LuN-1				–1.8
LuN-4			Chalcopyrite	–1.7
LuN-2				–1.7

to 19.133, $^{207}Pb/^{204}Pb$ = 15.564 to 15.665, and $^{208}Pb/^{204}Pb$ = 38.367 to 38.942. Initial Pb isotope ratios of these basalts at t = 232 Ma (the age of the ore deposit) have been calculated using the whole-rock Pb isotope ratios and whole-rock U, Th, and Pb contents, and are $(^{206}Pb/^{204}Pb)_t$ = 17.678 to 18.987, $(^{207}Pb/^{204}Pb)_t$ = 15.543 to 15.646, and $(^{208}Pb/^{204}Pb)_t$ = 38.175 to 38.659.

Four samples from the ore-hosting strata in the Yangla mining area (i.e., marble, quartz sandstone, and siliceous rock) have present-day $^{206}Pb/^{204}Pb$ ratios of 18.365 to 19.035, $^{207}Pb/^{204}Pb$ of 15.652 to 15.750, and $^{208}Pb/^{204}Pb$ of 38.515 to 39.394, and values at t = 232 Ma of $(^{206}Pb/^{204}Pb)_t$ = 18.300 to 18.873, $(^{207}Pb/^{204}Pb)_t$ = 15.648 to 15.726, and $(^{208}Pb/^{204}Pb)_t$ = 38.511 to 38.982.

The calculated initial Pb isotope ratios of granitoids at Yangla are $(^{206}Pb/^{204}Pb)_t$ =18.213 to 18.598, $(^{207}Pb/^{204}Pb)_t$ = 15.637 to 15.730, and $(^{208}Pb/^{204}Pb)_t$ = 38.323 to 38.791 (J.-J. Zhu et al., 2011).

Zhan et al. (1998) reported lead isotope compositions of samples of pyrite, pyrrhotite, and chalcopyrite from Yangla which are relatively homogeneous: $^{206}Pb/^{204}Pb$ = 18.273 to 18.369, $^{207}Pb/^{204}Pb$ = 15.627 to 15.677, and $^{208}Pb/^{204}Pb$ = 38.445 to 39.611 (Table 5). As shown in Figure 10, the sulfide data plot in the field of granitoids and wall-rock compositions, but are significantly different from the Pb isotope ratios of basalts.

Carbon and oxygen isotopes

Carbon and oxygen isotope compositions of calcite (n = 9) from the late ore stage and marble wall rock (n = 6) are presented in Table 6 and Figure 11. The compositions of marble samples show a positively correlated trend, from $\delta^{13}C$ = 1.2 and $\delta^{18}O$ = 10.8 (highest degree of alteration) to $\delta^{13}C$ = 4.3‰ and $\delta^{18}O$ = 23.9‰ (lowest degree of alteration). A positive correlation is also shown by C-O isotope compositions of

TABLE 5. Lead Isotope Data of Sulfides, Wall Rocks, and Basalt in the Yangla Cu Deposit

Sample no.	Mineral/rock	$^{208}Pb/^{204}Pb$	2σ	$^{207}Pb/^{204}Pb$	2σ	$^{206}Pb/^{204}Pb$	2σ	$(^{208}Pb/^{204}Pb)t$	$(^{207}Pb/^{204}Pb)t$	$(^{206}Pb/^{204}Pb)t$	Comment
L81-1	Pyrrhotite	38.466	–	15.628	–	18.273	–				Zhan et al. (1998)
L81-2	Chalcopyrite	38.474	–	15.634	–	18.301	–				
L128	Chalcopyrite	38.611	–	15.680	–	18.369	–				
L135	Chalcopyrite	38.574	–	15.675	–	18.316	–				
L184	Chalcopyrite	38.445	–	15.630	–	18.308	–				
L203-1	Pyrrhotite	38.597	–	15.668	–	18.315	–				
L203-2	Pyrite	38.561	–	15.659	–	18.312	–				
L266	Pyrite	38.469	–	15.629	–	18.280	–				
L57	Chalcopyrite	38.602	–	15.677	–	18.313	–				
L230	Pyrite	38.534	–	15.659	–	18.291	–				
B005-3	Marble	38.515	0.005	15.652	0.002	18.364	0.003	38.512	15.648	18.300	This study
B026	Siliceous rock	38.693	0.003	15.661	0.001	18.469	0.002	38.511	15.653	18.310	
B036-1	Metasandstone	39.394	0.006	15.750	0.002	18.992	0.003	38.608	15.726	18.519	
B019	Siliceous rock	39.166	0.003	15.700	0.001	19.035	0.001	38.982	15.692	18.873	
N-1	Basalt	38.367	0.000	15.649	0.000	18.829	0.000	38.175	15.611	18.081	
N-2		38.648	0.001	15.621	0.000	18.356	0.000	38.238	15.601	17.946	
N-3		38.568	0.001	15.595	0.000	18.282	0.000	38.398	15.587	18.119	
N-4		38.434	0.001	15.564	0.000	18.740	0.000	38.191	15.543	18.327	
N-5		38.942	0.000	15.665	0.000	18.619	0.000	38.659	15.617	17.678	
N-6		38.584	0.000	15.615	0.000	19.133	0.000	38.516	15.608	18.987	
N-7		38.528	0.000	15.621	0.000	18.367	0.000	38.428	15.616	18.268	
S-1		38.775	0.000	15.657	0.000	18.734	0.000	38.500	15.646	18.521	

Notes: Initial Pb isotope ratios are calculated at t = 232 Ma; U, Th, and Pb contents are from our manuscript in preparation

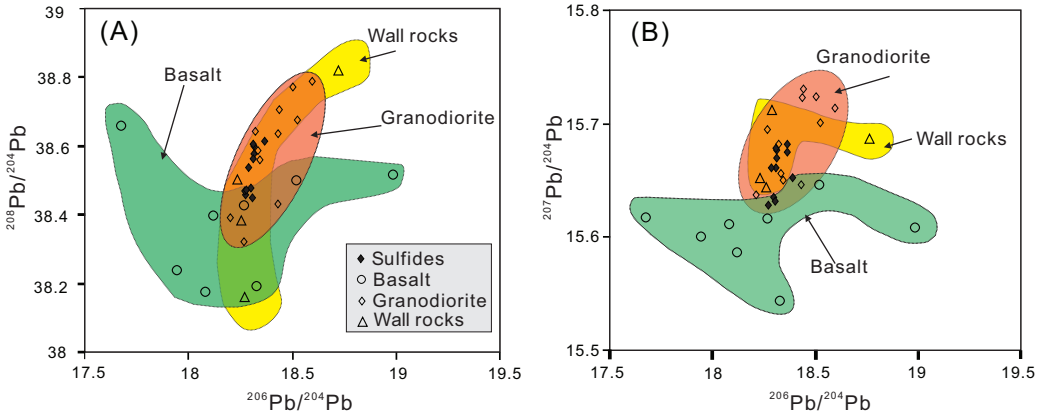

FIG. 10. Lead isotope compositions of basalts, granodiorites, and wall rocks from the Yangla Cu deposit, compared to data for sulfides (from Zhan et al., 1998) on (A) $^{208}Pb/^{204}Pb$ vs. $^{206}Pb/^{204}Pb$ and (B) $^{207}Pb/^{204}Pb$ vs. $^{206}Pb/^{204}Pb$ diagrams.

TABLE 6. Carbon-Oxygen Isotope Data of Calcites and Marble in the Yangla Cu Deposit

Sample no.	Mineral/rock	$\delta^{13}C_{PDB}$ (‰)	$\delta^{18}O_{V\text{-}SMOW}$ (‰)	$\delta^{13}C_{fluid}$ (‰)[1]	$\delta^{18}O_{fluid}$ (‰)[2]	Comment
083075-29	Calcites in the	–5.9	7.2	–4.6	0.5	Interstitial calcites between diopside crystals
083250-15	early substage	–5.5	12.0	–4.2	5.3	
093075-1		–5.6	18.0	–4.3	11.2	
083225-4	Calcites in the	–3.7	17.8	–2.5	11.0	Calcite veins (~10 cm wide and ~20 m long)
093250-3	late substage	–3.6	15.7	–2.3	8.9	
083050-1		–3.5	18.0	–2.2	11.2	
093075-11		–3.4	16.6	–2.2	9.8	
083250-18		–3.4	16.7	–2.1	9.9	
103175-3		–3.2	14.9	–2.0	8.1	
B002	Marble	2.0	21.6			Lowest degree alteration
B005-3		4.0	18.8			Highest degree alteration
083075-1		4.3	23.9			
B043		1.2	10.8			
093200-8		3.6	19.4			
083250-3		4.2	19.4			

Notes: All the calculations are based on T = 250°C from fluid inclusion analysis; see text for details of method for calculating C-O isotope compositions of the ore-forming fluid

[1] $\delta^{13}C$ values of fluids in equilibrium with calcite were calculated using equations of Bottinga (1968): $1{,}000\ln\alpha_{(CO2\text{-}Calcite)} = -2.4612 + 7.663 \times 10^3/T - 2.9880 \times 10^6/T^2$

[2] Calculated using the fractionation factors between calcite-water (O'Neil et al., 1969): $1{,}000\ln\alpha_{(Calcite\text{-}Water)} = 2.78 \times 10^6/T^2 - 3.39$

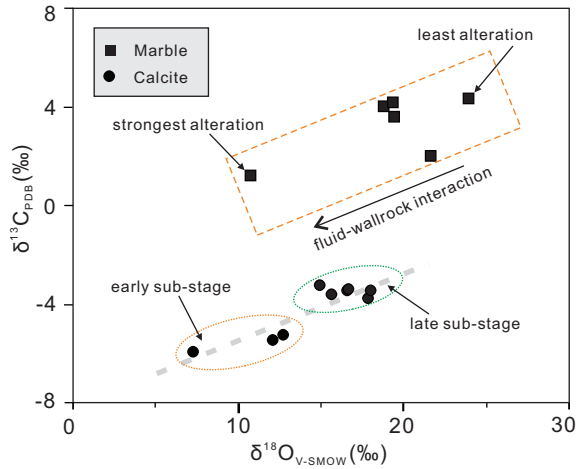

FIG. 11. $\delta^{13}C$ vs. $\delta^{18}O$ data for late ore stage vein calcites and marble wall rocks in the Yangla Cu deposit. Note two substages of calcites.

calcites (Fig. 11), from $\delta^{13}C$ = –5.9‰ and $\delta^{18}O$ = 7.2‰ to $\delta^{13}C$ = –3.5‰ and $\delta^{18}O$ = 18.0‰. Calcites from the early substage have lower isotopic ratios ($\delta^{13}C$ = –5.9 to –5.6‰, $\delta^{18}O$ = 7.2 to 18.0‰) than calcites from the late substage ($\delta^{13}C$ = –3.7 to –3.2‰, $\delta^{18}O$ = 14.9 to 18.0‰).

Calcite is the main carbon-bearing mineral in the deposit and no graphite occurs in the ore field. Therefore, temperature-corrected calcite carbon isotope compositions likely reflect the bulk C isotope composition of the late ore fluid, and can potentially be used as a tracer for the source of carbon (Ohmoto and Goldhaber, 1997). Using a temperature of 250°C (estimated from fluid inclusion analyses in calcite; see below), calculated $\delta^{13}C_{fluid}$ values for early substage calcites range from –4.6 to –4.2‰ (average = 4.4 ± 0.2‰, n = 3, using the CO_2-calcite fractionation equation of Bottinga, 1968; Table 6). Calculated $\delta^{18}O_{fluid}$ values range from 0.5 to 11.2‰, with an average of 5.7 ± 5.4‰ (n = 3; using the H_2O-calcite fractionation equation of O'Neil et al., 1969; Table 6).

For the late substage, calculated $\delta^{13}C_{fluid}$ values (also using 250°C) are from –2.5 to –2.0‰ (average = –2.2 ± 0.2‰, n = 6), and $\delta^{18}O_{fluid}$ values from 8.1 to 11.2‰ (average = 9.8 ± 1.2‰, n = 6).

Fluid Inclusion Studies

Fluid inclusion types

Three types of primary fluid inclusions were recognized in several kinds of minerals from Yangla: hypersaline inclusions (H) with halite (30–40 vol %) and other daughter crystals at room temperature, and relatively large vapor bubbles (20–40 vol %; Fig. 12A-D); liquid-rich inclusions (L) with relatively small vapor bubbles (10–20 vol %; Fig. 12E, F); and vapor-rich inclusions (V; more than 80 vol % vapor; Fig. 12B, C).

The hypersaline inclusions commonly occur with vapor-rich inclusions (H + V assemblages) and are typically present in pre-ore stage diopside and andradite. These inclusions generally occur in negative crystal shapes and range from 10 to 30 μm in size (Fig. 12A-D). These H-type inclusions were more abundant in diopside than andradite, as has been noted

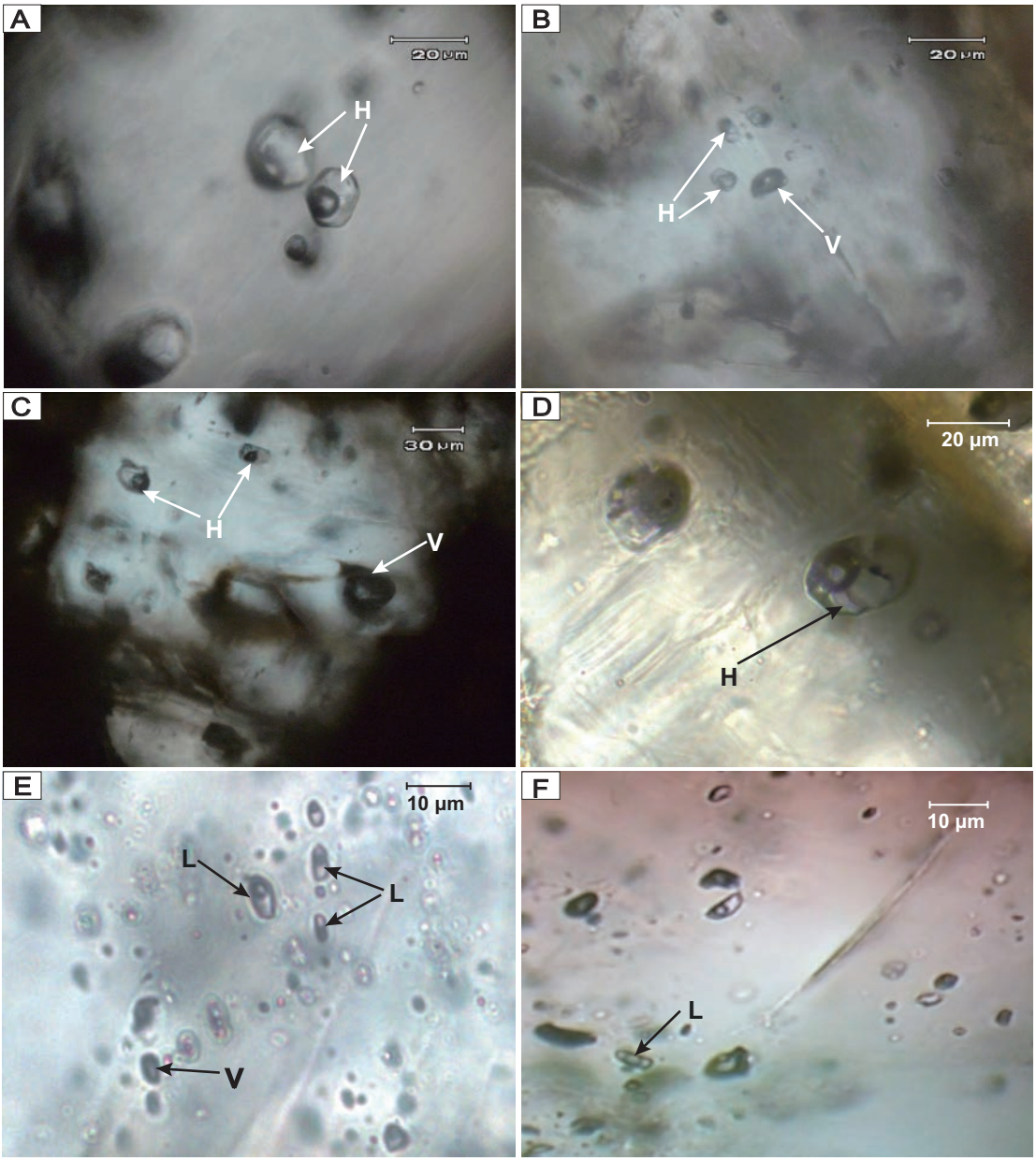

FIG. 12. Primary fluid inclusion types in different stages. (A) Hypersaline (H) inclusions in pre-ore stage diopside (sample 3200-25-1). (B) and (C) Coexistence of vapor-rich (V) and hypersaline inclusions in diopside (sample 3200-26). (D) Hypersaline inclusions in diopside. Note that there are unknown daughter minerals (dark) nearby the halite crystal. (E) Coexisting vapor- and liquid-rich (L) inclusions in quartz of main ore stage (sample 3075-2). (F) Liquid-rich inclusions in late-stage calcite (sample 3200-25-1); note that the dark-looking fluid inclusions are not vapor-rich ones but inclusions in different depth of focus.

in several other skarn deposits (e.g., Meinert et al., 1997; Shu et al., 2013).

Liquid-rich (L type) inclusions typically occur in main ore stage quartz (Fig. 12E) and late ore stage calcite (Fig. 12F). They were much smaller in size (5–10 μm in quartz and ~5 μm in calcite) than those in diopside and andradite, with oval and negative crystal shapes. Vapor-rich (V type) inclusions were also detected in main ore stage quartz, but rarely in late ore stage calcite.

Microthermometric observations

The results of fluid inclusion salinity and homogenization temperature measurements are summarized in Table 7 and illustrated in Figures 13 and 14. Only primary inclusions were analyzed for this study, based on the criteria of Roedder (1984). Other inclusions were avoided, including those that showed evidence of necking or leaking, and those located within areas showing recrystallization textures. As noted above, diopside and minor garnet host pre-ore stage H + V inclusions, whereas quartz (intergrown with chalcopyrite and molybdenite) in veins contains numerous main ore stage L + V inclusions. Late ore stage calcite veinlets contain mainly L-type fluid inclusions. All the H- and L-type inclusions homogenized to the liquid phase during heating, with daughter minerals dissolving before bubble disappearance in H-type inclusions. Although V-type inclusions are widespread in the pre-ore and main ore stages, poor visibility meant that it was difficult to measure either ice-melting or homogenization temperatures in these inclusions.

Pre-ore stage: Thirty-three H-type fluid inclusions, of which 31 were hosted by diopside and two in andradite (samples 3200-25-1 and 3200-26), had halite dissolution temperatures ranging from 387° to 453°C. Salinities calculated from these inclusions have a range from 46.1 to 53.7 wt % NaCl equiv (average = 49.4 ± 1.7 wt % NaCl equiv, n = 33; Fig. 13B). They homogenized by bubble disappearance, with a range of final homogenization temperatures from 508° to >600°C (mostly between 560° and 600°C; Fig. 13A; Table 7). The densities of these fluid inclusions are estimated to be 0.930 to 1.026 g/cm^3 (Table 7) using the program of Mao and Duan (2008).

Vapor-rich (V type) fluid inclusions commonly occur together with H-type inclusions (Fig. 12B, C), implying two-phase fluid conditions during trapping. As noted above, it was very difficult to determine salinities and homogenization temperatures for these inclusions. However, a few V-type inclusions were occasionally found that did not homogenize below 600°C (the upper temperature limit of the microthermometric stage).

Main ore stage: Liquid-rich fluid inclusions are the most abundant type in main ore stage quartz (samples 3075-2, 3075-2-1, 3075-37, and 3250-9), defining a relatively tightly

Table 7. Summary of Microthermometric Data of Fluid Inclusions from the Yangla Cu Deposit

Stage	Host mineral	Fluid inclusion type[1]	Final melting temperature of ice[2]	Dissolution temperature of halite	Homogenization temperature[3]	Salinity (wt % NaCl equiv)	Density (g/cm^3)
Pre-ore	Andradite	H, V		398 to 424.5 (2)	567 to 599 (2)	47.2 to 50.2	0.930 to 0.983
	Diopside	H, V		387.0 to 453.2 (31)	508 to over 600 (24)	46.1 to 53.7	0.943 to 1.026
Main ore	Quartz-1	L, V	–1.9 to –3.4 (14)		312.0 to 389.0 (20)	2.41 to 5.56	0.591 to 0.731
Late ore	Quartz-2	L	–2.3 to –5.1 (4)		220.0 to 283.2 (4)	3.87 to 8.00	0.795 to 0.878
	Calcite	L	–1.2 to –2.3 (7)		224.5 to 290.0 (10)	2.07 to 3.87	0.775 to 0.864

Note: See text for detailed methods for calculating salinity and density
[1] Fluid inclusion type: H = hypersaline, L= liquid rich, V = vapor rich; no data are from V-type inclusions
[2] The number in parentheses denotes number of measurements
[3] Temperature values are reported in °C

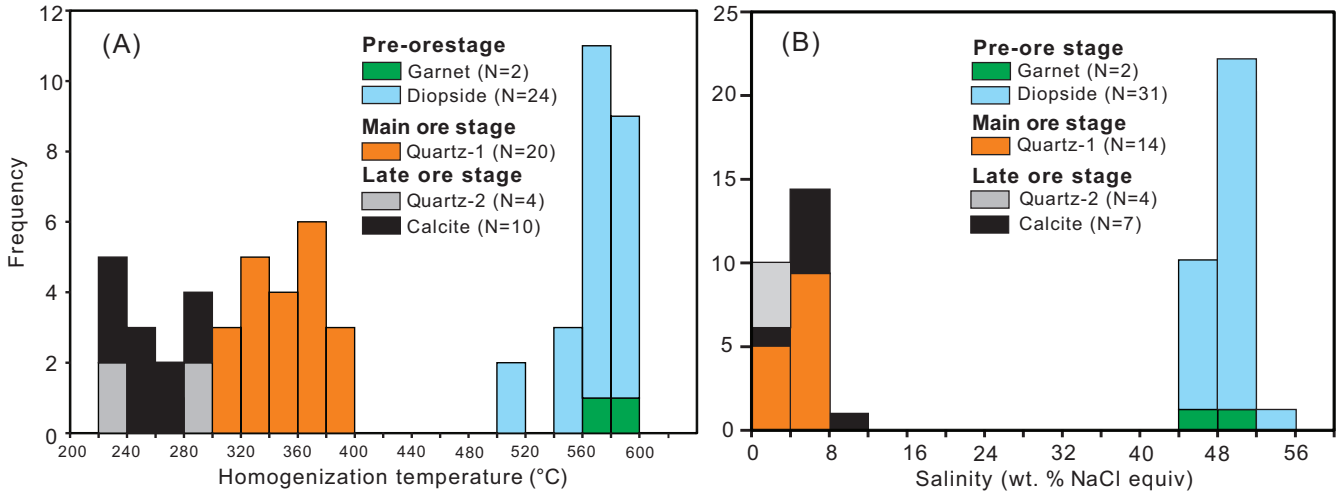

Fig. 13. Homogenization temperature (A) and salinity (B) histograms for all inclusion types separated into different stages and host minerals.

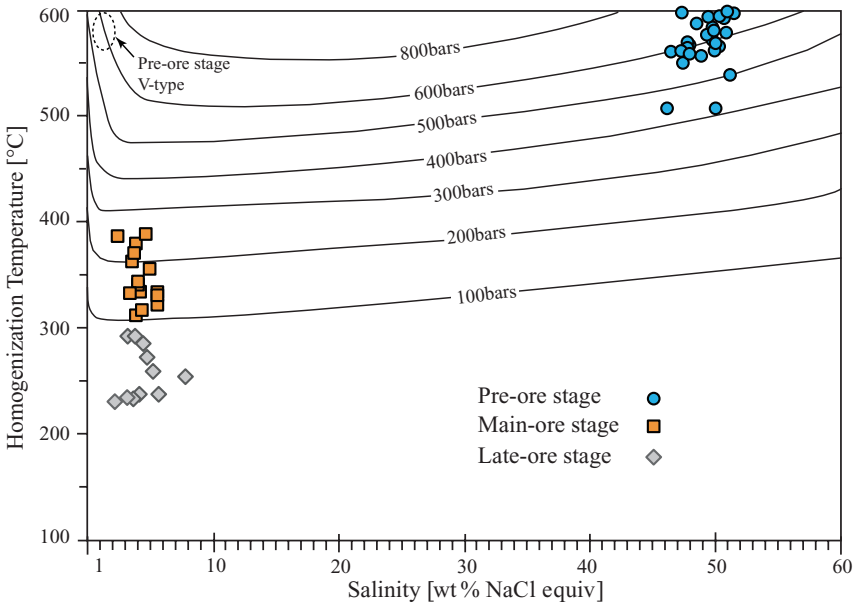

FIG. 14. Summary plot of homogenization temperatures and salinities of individual fluid inclusions of different stages for the Yangla Cu deposit. Note that the salinities for pre-ore stage V-type inclusions are inferred. Pre- and main ore stage fluid inclusion assemblages were trapped under two-phase conditions, and isobars (calculated from the equations of Driesner and Heinrich, 2007) can be used to estimate pressure conditions for these fluids (assuming simple NaCl-H_2O solutions).

grouped population with homogenization temperatures ranging from 312° to 389°C (average = 350 ± 24.7°C, n = 20; Fig. 13A). Ice-melting temperatures for 14 of these inclusions are between –1.4° and –3.4°C, corresponding to salinities from 2.4 to 5.6 wt % NaCl equiv (average = 4.2 ± 0.9 wt % NaCl equiv, n = 13; Fig. 13B). Densities of these fluid inclusions are much lower than in the pre-ore stage, ranging from 0.614 to 0.738 g/cm^3 (Table 7).

Vapor-rich fluid inclusions were present with liquid-rich inclusions in some assemblages (Fig. 12E). As for vapor-rich fluid inclusions in diopside and andradite, no ice-melting or homogenization temperatures could be obtained for these inclusions. However, coexistence of fluid inclusions representing trapped vapor and liquid phases indicates that the system formed close to or on the two-phase line. We therefore suggest that boiling continued during the main ore stage.

Late ore stage: Liquid-rich fluid inclusions are the only type recognized in late ore stage (both early and late substages) calcite (samples 3050-18, 3075-22, and 3200-25-1) and quartz (sample 3075-2-1) veins. Eleven inclusions gave homogenization temperatures ranging from 220° to 290°C (average = 249 ± 27°C, n = 14; Fig. 13A). Ice-melting temperatures varied from –1.2° to –5.1°C, equivalent to salinities of 2.1 to 8.0 wt % NaCl equiv (average = 4.6 ± 1.5 wt % NaCl equiv, n = 11; Fig. 13B) and densities between 0.775 and 0.878 g/cm^3 (Table 7). Clear evidence of boiling was not observed in this stage.

Pressure estimation

Estimates of trapping pressure can be conducted only when the actual trapping temperature is known, or if boiling was occurring in the system at the time of entrapment (Roedder and Bodnar, 1980). As described above, evidence of boiling was observed in both the pre- and main ore stages and, thus, homogenization temperatures are interpreted to closely approximate trapping temperatures. Trapping pressures can also be estimated. Lack of evidence for boiling in the late ore stage only permits the estimation of minimum trapping temperatures and pressures for the late fluids.

Assuming that the fluids can be represented as a simple NaCl-H_2O system, isobar equations from Driesner and Heinrich (2007) were used to estimate trapping pressures in the pre- and main ore stages. As shown in Figure 14, the estimated trapping pressures for H-type fluid inclusions of the pre-ore stage are concentrated at ~600 bars. For the coexisting V- and L-type inclusions of the main ore stage, trapping pressures are estimated ranging from 100 to 300 bars, with an average of ~200 bars. These pressures are equivalent to a trapping depth of ~2 km if lithostatic pressures are assumed in the high-temperature pre-ore stage, and hydrostatic pressures in the lower-temperature main ore stage.

Discussion

Timing and genesis of the Yangla Cu deposit

Timing: The mineralization age of the Yangla Cu deposit is well constrained by Re-Os dating of molybdenite (isochron age: 232.0 ± 1.5 Ma at 2σ; weighted average age = 231.8 ± 1.3 Ma, 95% confidence level; Fig. 8). It is coeval within error with the crystallization age of the associated Jiaren granitoids in the ore field (233.1 ± 1.4 Ma at 2σ, 231.0 ± 1.6 Ma at 2σ; J.-J. Zhu et al., 2011). Depicted using our previously published data (J.-J. Zhu et al., 2011), diagrams of Y vs. Nb and Rb vs. (Nb + Y) both show that these granodiorite rocks are in accord with those of typical skarn Cu deposits worldwide (Fig. 15; Meinert, 1995), implying that the Cu mineralization was probably related to the granitic magmatism.

Although most porphyry copper systems are found above active subduction zones at convergent plate margins (e.g.,

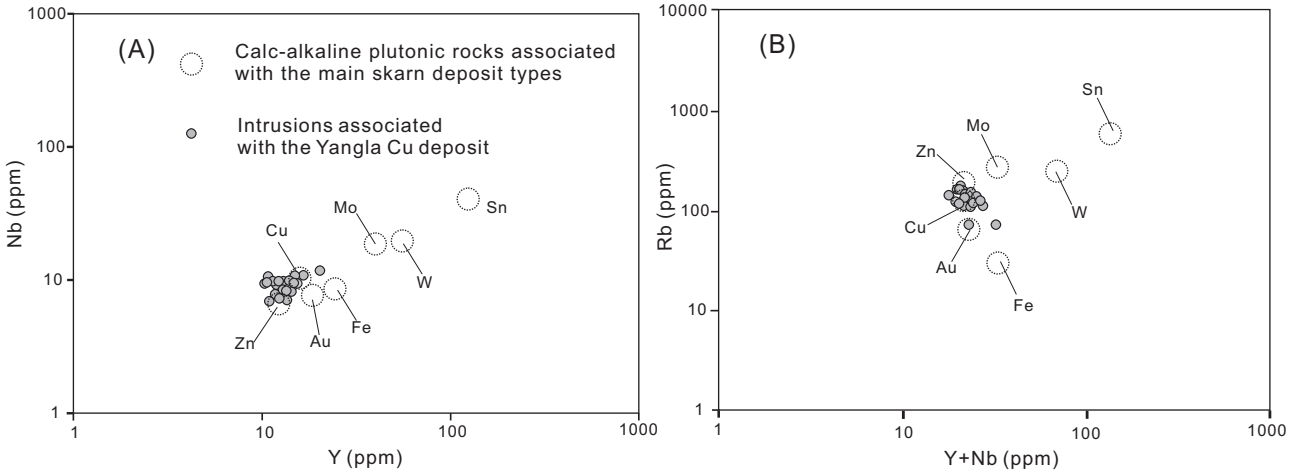

FIG. 15. (A) Nb vs. Y and (B) Rb vs. (Nb + Y) correlation diagrams for granitoids associated with Cu mineralization at Yangla (data from J.-J. Zhu et al., 2011), and average compositions of plutons associated with skarn deposit types worldwide (Meinert, 1995).

Sillitoe, 1972, 2010), numerous porphyry copper, epithermal gold, and skarn deposits postdating the termination of oceanic subduction have been documented in the Tethys orogenic belt (e.g., the Sari Gunay epithermal Au deposit in Iran, Richards et al., 2006; Richards, 2009; the Çöpler epithermal Au deposit in Turkey, Keskin et al., 2008; Imer et al., 2013; the Gangdese belt in Tibet, J.-X. Li et al., 2011; Hou et al., 2013; R. Wang et al., 2014a, b). Magmatism and hydrothermal activity at Yangla occurred at ~232 Ma, also significantly postdating Early Triassic collision (246–247 Ma; Zi et al., 2012b) between the Qamdo-Simao terrane and the Zhongza terrane along the Jinshajiang suture, following the closure of the Jinshajiang Paleo-Tethys Ocean (Fig. 1). Thus, perhaps more attention should be paid to regions of postsubduction magmatism in the Sanjiang metallogenic domain, which also have the potential to host significant porphyry and skarn copper deposits.

Sources of sulfur and lead: Sulfur isotopes of chalcopyrite (which are thought to reflect the bulk sulfur isotope composition of the fluid) show a narrow range from $\delta^{34}S$ = –1.8 to +1.8‰. It is suggested the Yangla Cu deposit has a solely magmatic source of sulfur (–3 to +1‰; Hoefs, 2009), consistent with formation as a skarn deposit.

Sulfide samples are characterized by relatively homogeneous Pb isotope compositions, which are broadly comparable with values for the associated granitoids and wall rocks, but distinct from those of basalts (Fig. 10). We therefore suggest that the granitic magma and host rocks contributed most of the lead and ore-forming metals, whereas Carboniferous basalt has made little contribution to the mineralization. This coincides well with the observation that most of the mineralization occurs in the contact zone between granodiorite and sedimentary wall rocks.

Source of ore-forming fluid: Calculated $\delta^{13}C_{fluid}$ values for early substage calcites range from –4.6 to –4.2‰ (average = 4.4 ± 0.2‰, n = 3), which are consistent with the C isotope compositions of mantle-derived rocks (–5 ± 2‰; Ohmoto and Rye, 1979); their calculated $\delta^{18}O_{fluid}$ values range from 0.5 to 11.2‰, with an average of 5.7 ± 5.4‰ (n = 3), generally coinciding with that of magmatic water (6–10‰; Hoefs, 2009). The C-O isotope ratios of calcites and related fluid both increase from the early to late substage. Calculated $\delta^{13}C_{fluid}$ values are from –2.5 to –2.0‰ (average = –2.2 ± 0.2‰, n = 6) and $\delta^{18}O_{fluid}$ values are from 8.1 to 11.2‰ (average = 9.8 ± 1.2‰, n = 6) in the late substage, which are slightly higher than those of typical magmatic water. The C-O isotope compositions indicate that the ore-forming fluid was predominantly of magmatic origin, but it might have isotopically exchanged with the carbonate country rocks (marbles), which have higher C-O isotope ratios ($\delta^{13}C$ = 1.2–4.3‰; $\delta^{18}O$ = 7.2–18.0‰) during the late substage.

Fluid-rock interaction is supported by the $\delta^{13}C$ and $\delta^{18}O$ values of marble, which show a strong correlation with the degree of alteration (both values decrease with intensity of alteration; Fig. 11). This isotopic shift is interpreted to reflect the interaction between magmatic fluids and the carbonate country rocks.

However, both C and O isotope fractionation factors between calcite and fluid increase with decreasing temperature (Bottinga, 1968; O'Neil et al., 1969). The ore-forming fluid in the late substage was likely cooler (although we chose the same temperature for both the early and late substages), which might be also responsible for its lower calculated C-O isotope ratios.

Based on field, textural, mineralogical, geochemical, geochronological, and isotopic studies, we therefore conclude that the Yangla Cu deposit is a typical Cu skarn system, related to the Late Triassic Jiaren granitoids.

Fluid processes and ore precipitation

Fluid processes: Fluid evolution of the Yangla Cu deposit is illustrated in Figure 16. As the Jiaren granitoid pluton cooled and crystallized, we suggest that an initially supercritical fluid with a salinity of 6 to 8 wt % NaCl equiv exsolved from the magma chamber (Burnham, 1979; Hedenquist and Lowenstern, 1994). Rapid ascent to a depth of ~2 km (~600 bars; lithostatic pressure conditions) caused this fluid to intersect its solvus at a temperature of ~560° to 600°C and to condense

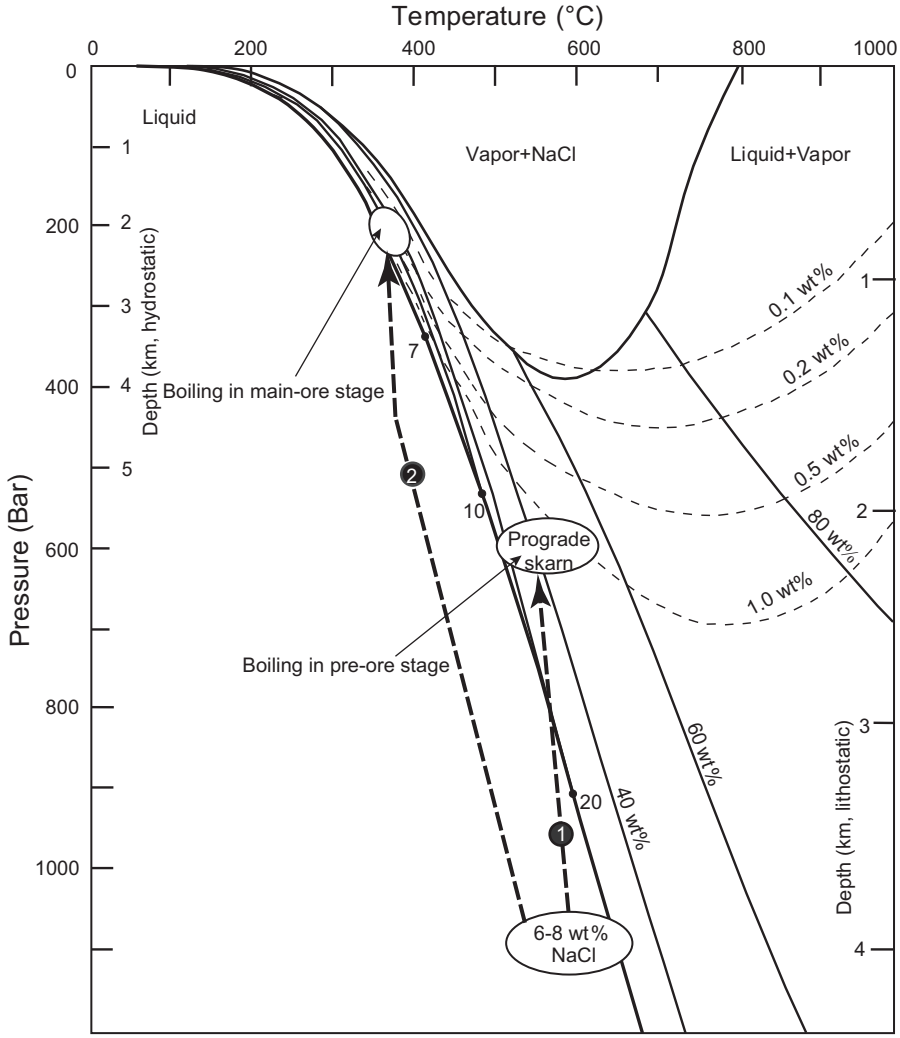

FIG. 16. Possible fluid evolution paths for the Yangla Cu deposit (after Fournier, 1987; Hedenquist et al., 1998). The initial fluids for the pre- and main ore stages are both suggested to be supercritical magmatic fluids with an initial salinity of 6 to 8 wt % NaCl equiv (Burnham, 1979; Hedenquist and Lowenstern, 1994). These fluids followed different cooling paths: in the pre-ore stage (path 1), the trajectory intersects the solvus above ~560°C and at a pressure of ~600 bars (lithostatic depth of ~2 km); in the main ore stage (path 2), the trajectory intersects the solvus below ~390°C and at a pressure of ~200 bars (~2 km; hydrostatic conditions). For details see text.

a saline liquid phase (~49 wt % equiv NaCl; Fig. 13) from a lower-density vapor (path 1 in Fig. 16). These conditions are recorded by fluid inclusions trapped in prograde (pre-ore stage) skarn minerals (andradite and diopside), and are typical of skarn deposits worldwide (Meinert et al., 1997, 2003; Baker and Lang, 2003; Chang and Meinert, 2008; Shu et al., 2013).

Fluid inclusions in main ore stage quartz also record boiling conditions, but the liquid phase is cooler (312°–389°C) and more dilute (2.4–5.6 wt % NaCl equiv; Figs. 13, 14). We suggest that this fluid is also of magmatic origin, but it ascended and cooled more slowly such that it did not intersect its solvus curve until lower temperatures and pressures (~200 bars; ~2 km under hydrostatic pressure conditions; path 2 in Fig. 16; Hedenquist et al., 1998). These conditions attended the main stage of sulfide ore formation and retrograde skarn alteration.

Calcite in late ore stage veinlets contains nonboiling fluid inclusion assemblages with lower homogenization temperatures (average = 249° ± 27°C, n = 14; Fig. 13A) but similar salinities (average = 4.6 ± 1.5 wt % NaCl equiv, n = 11; Fig. 13B), suggesting that these fluids may simply be the cooled equivalent of the main ore stage fluid.

The absence of mixing trends in the fluid inclusion data, combined with stable isotopic evidence, suggests that fluid mixing with meteoric water was insignificant throughout the hydrothermal evolution of the deposit.

Ore precipitation: A variety of ore deposition processes might be invoked at Yangla. Firstly, the pH value of ore-forming fluid would have increased by reaction with the carbonate country rocks, which would reduce the solubility of Cu (Brimhall and Crerar, 1987). Secondly, temperature decreased from 560° to 600°C in the pre-ore stage to 312° to 389°C in the main ore stage, with a sharp decrease in salinity from ~49.4 to ~4.2 wt % (Fig. 14). Experimental studies indicate that Cu solubility decreases with decreasing temperature and salinity (Hemley et al., 1992). In addition, fluid boiling is suggested to have occurred in the main ore stage. Phase separation would increase the Cu concentration in the ore-forming fluid (Cline, 2003; Harris et al., 2003). Geochemical modeling based on LA-ICP-MS analysis of fluid inclusions may assess what the most important mechanisms are for precipitation (Bertelli et al., 2009), but the available data suggest the ore deposition could be readily initiated by all of processes above in concert.

Conclusions

The Yangla Cu deposit formed at ~232 Ma, coeval with the emplacement of spatially related granitoids. Sulfur, carbon,

and oxygen stable isotope compositions indicate that the ore-forming components were of magmatic origin. Lead isotope compositions of sulfides are similar to those of the granitoids and host rocks, consistent with a magmatic source for Pb and perhaps other metals. In combination, these characteristics suggest that Yangla is a typical Cu skarn deposit.

Two stages of fluid boiling were observed by detailed fluid inclusion study:

1. Pre-ore stage: Coexistence of brine and vapor in the this stage suggests that fluid boiling occurred at about 2 km (560°–600°C, ~600 bars, lithostatic pressure conditions), and the resulting high-salinity liquid (average = 49.4 ± 1.7 wt % NaCl equiv, n = 33) was preserved as fluid inclusions in prograde skarn minerals (diopside and andradite).

2. Main ore stage: Fluid boiling in the main ore stage was identified by the coexistence of vapor-rich and liquid-rich fluid inclusions trapped at a temperature of 350° ± 24.7°C (n = 20) and at a depth of ~2 km (~200 bars, hydrostatic pressure conditions), which was associated with the retrograde skarn alteration and mineralization.

Acknowledgments

This study was jointly supported by the National Natural Science Foundation Project of China (41303040), the National Key Basic Research Program of China (2014CB440902), the CAS/SAFEA International Partnership Program for Creative Research Teams (Intraplate Mineralization Research Team: KZZD-EW-TZ-20), and the Frontier Program of the State Key Laboratory of Ore-Deposit Geochemistry, Chinese Academy of Sciences, and was conducted while the first author was a visiting scientist at the University of Alberta. We thank Fei Long, Yue-dong Liu, and Cheng Luo from the Yunnan Copper (Group) Corporation and Dr. Heng Chen, Lei-luo Xu, and You-wei Chen from the Institute of Geochemistry, Chinese Academy of Sciences (IGCAS) for help with the field work. We also appreciate the kind help of Dr. Andrew Locock from the University of Alberta and Ms. Wen-qin Zheng from IGCAS on EPMA analysis, Chao Li from Chinese Academy of Geological Sciences on Re-Os isotope dating, and Dr. Lian Zhou from China University of Geosciences at Wuhan and Ning An from IGCAS on stable isotope analysis. Thanks to Mr. Rui Wang from University of Alberta and Dr. Jin-xiang Li from the Institute of Tibetan Plateau Research, Chinese Academy of Sciences for constructive comments on the original manuscript.

REFERENCES

Baker, T., and Lang, J.R., 2003, Reconciling fluid inclusion types, fluid processes, and fluid sources in skarns: An example from the Bismark deposit, Mexico: Mineralium Deposita, v. 38, p. 474–495.

Bertelli, M., Baker, T., Cleverley, J.S., and Ulrich, T., 2009, Geochemical modelling of a Zn-Pb skarn: Constraints from LA-ICP-MS analysis of fluid inclusions: Journal of Geochemical Exploration, v. 102, p. 13–26.

Bi, X., Hu, R., and Cornell, D., 2004, The alkaline porphyry associated Yao'an gold deposit, Yunnan, China: Rare earth element and stable isotope evidence for magmatic-hydrothermal ore formation: Mineralium Deposita, v. 39, p. 21–30.

Bottinga, Y., 1968, Calculation of fractionation factors for carbon and oxygen isotopic exchange in the system calcite-carbon dioxide-water: Journal of Physical Chemistry, v. 72, p. 800–808.

Boulin, J., 1991, Structures in southwest Asia and evolution of the eastern Tethys: Tectonophysics, v. 196, p. 211–268.

Brimhall, G.H., and Crerar, D.A., 1987, Ore fluids; magmatic to supergene: Reviews in Mineralogy and Geochemistry, v. 17, p. 235–321.

Burnham, C.W., 1979, Magmas and hydrothermal fluids, *in* Barnes H.L., ed., Geochemistry of hydrothermal ore deposits, 2nd edition: New York, John Wiley and Sons, p. 71–136.

Calagari, A.A., and Hosseinzadeh, G., 2006, The mineralogy of copper-bearing skarn to the east of the Sungun-Chay River, East-Azarbaidjan, Iran: Journal of Asian Earth Sciences, v. 28, p. 423–438.

Chang, Z., and Meinert, L.D., 2008, The Empire Cu-Zn mine, Idaho: Exploration implications of unusual skarn features related to high fluorine activity: Economic Geology, v. 103, p. 909–938.

Chen, S.Y., Gu, X.X., Cheng, W.B., Zheng, G., Han, S.Y., and Peng, Y.W., 2013, Characteristics of ore-forming fluid and mineralization process of the Yangla copper deposit, Yunnan: Earth Science Frontiers, v. 20, p. 82–91 (in Chinese with English abstract).

Cline, J.S., 2003, How to concentrate copper: Science, v. 302, p. 2075–2076.

Coplen, T.B., Kendall, C., and Hopple, J., 1983, Comparison of stable isotope reference samples: Nature, v. 302, p. 236–238.

Deng, J., Wang, Q., Li, G., Li, C., and Wang, C., 2014, Tethys tectonic evolution and its bearing on the distribution of important mineral deposits in the Sanjiang region, SW China: Gondwana Research, v. 26, 419–437.

Ding, T.P., Valkiers, S., Wan, D.F., Bai, R.M., Zou, X.Q., Li, Y.H., Zhang, Q.L., and Bievre, P.D., 2001, The $\delta^{33}S$ and $\delta^{34}S$ values and absolute $^{32}S/^{33}S$ and $^{32}S/^{34}S$ ratios of IAEA and Chinese sulfur isotope reference materials: Bulletin of Mineralogy, Petrology and Geochemistry, v. 20, p. 425–427 (in Chinese with English abstract).

Driesner, T., and Heinrich, C.A., 2007, The system H_2O-NaCl. Part I: Correlation formulae for phase relations in temperature-pressure-composition space from 0 to 1000°C, 0 to 5000bar, and 0 to 1 X_{NaCl}: Geochimica et Cosmochimica Acta, v. 71, p. 4880–4901.

Drobe, J., Lindsay, D., Stein, H., and Gabites, J., 2013, Geology, mineralization, and geochronological constraints of the Mirador Cu-Au porphyry district, southeast Ecuador: Economic Geology, v. 108, p. 11–35.

Du, A., Wu, S., Sun, D., Wang, S., Qu, W., Markey, R., Stain, H., Morgan, J., and Malinovskiy, D., 2004, Preparation and certification of Re-Os dating reference materials: Molybdenites HLP and JDC: Geostandards and Geoanalytical Research, v. 28, p. 41–52.

Einaudi, M.T., and Burt, D.M., 1982, Introduction—terminology, classification, and composition of skarn deposits: Economic Geology, v. 77, p. 745–754.

Fan, W., Wang, Y., Zhang, A., Zhang, F., and Zhang, Y., 2010, Permian arc—back-arc basin development along the Ailaoshan tectonic zone: Geochemical, isotopic and geochronological evidence from the Mojiang volcanic rocks, southwest China: Lithos, v. 119, p. 553–568.

Foley, S.F., and Wheller, G.E., 1990, Parallels in the origin of the geochemical signatures of island arc volcanics and continental potassic igneous rocks: The role of residual titanites: Chemical Geology, v. 85, p. 1–18.

Fournier, R.O., 1987, Conceptual models of brine evolution in magmatic hydrothermal systems: U.S. Geological Survey Professional Paper 1350, p. 1487–1506.

Franklin, J., Gibson, H., Jonasson, I., and Galley, A., 2005, Volcanogenic massive sulfide deposits: Economic Geology 100th Anniversary Volume, v. 98, p. 523–560.

Gan, J.M., Zhan, M.G., Yu, F.M., He, L.Q., Chen, S.F., and Dong, F.L., 1998, Structural deformation and its ore-control significance in Yangla copper district, Deqing, western Yunnan: Geology and Mineral Resources of South China, v. 4, p. 59–65 (in Chinese with English abstract).

Hall, D.L., Sterner, S.M., and Bodnar, R.J., 1988, Freezing point depression of NaCl-KCl-H_2O solutions: Economic Geology, v. 83, p. 197–202.

Harris, A.C., Kamenetsky, V.S., White, N.C., Van Achterbergh, E., and Ryan, C.G., 2003, Melt inclusions in veins: Linking magmas and porphyry Cu deposits: Science, v. 302, p. 2109–2111.

Haynes, F.M., 1985, Determination of fluid inclusion compositions by sequential freezing: Economic Geology, v. 80, p. 1436–1439.

Hedenquist, J.W., and Lowenstern, J.B., 1994, The role of magmas in the formation of hydrothermal ore deposits: Nature, v. 370, p. 519–527.

Hedenquist, J.W., Arribas, A., and Reynolds, T.J., 1998, Evolution of an intrusion-centered hydrothermal system: Far Southeast-Lepanto porphyry and epithermal Cu-Au deposits, Philippines: Economic Geology, v. 93, p. 373–404.

Hemley, J., Cygan, G., Fein, J., Robinson, G., and d'Angelo, W., 1992, Hydrothermal ore-forming processes in the light of studies in rock-buffered systems: I. Iron-copper-zinc-lead sulfide solubility relations: Economic Geology, v. 87, p. 1–22.

Hoefs, J., 2009, Stable isotope geochemistry, 6th ed.: Berlin Heidelberg, Springer-Verlag, 285 p.

Hou, Z.Q., Ma, H., Zaw, K., Zhang, Y., Wang, M., Wang, Z.W., Pan, G.P., and Tang, R., 2003, The Himalayan Yulong porphyry copper belt: Product of large-scale strike-slip faulting in eastern Tibet: Economic Geology, v. 98, p. 125–145.

Hou, Z.Q., Zaw, K., Pan, G., Mo, X., Xu, Q., Hu, Y., and Li, X., 2007, Sanjiang Tethyan metallogenesis in S.W. China: Tectonic setting, metallogenic epochs and deposit types: Ore Geology Reviews, v. 31, p. 48–87.

Hou, Z.Q., Zheng, Y., Yang, Z., Rui, Z., Zhao, Z., Jiang, S., Qu, X., and Sun, Q., 2013, Contribution of mantle components within juvenile lower-crust to collisional zone porphyry Cu systems in Tibet: Mineralium Deposita, v. 48, p. 173–192.

Hu, R.Z., Burnard, P., Turner, G., and Bi, X.W., 1998, Helium and argon isotope systematics in fluid inclusions of Machangqing copper deposit in west Yunnan Province, China: Chemical Geology, v. 146, p. 55–63.

Imer, A., Richards, J.P., and Creaser, R.A., 2013, Age and tectonomagmatic setting of the Eocene Çöpler-Kabataş magmatic complex and porphyry-epithermal Au deposit, east central Anatolia, Turkey: Mineralium Deposita, v. 48, p. 557–583.

Jian, P., Liu, D., and Sun, X., 2008, SHRIMP dating of the Permo-Carboniferous Jinshajiang ophiolite, southwestern China: Geochronological constraints for the evolution of Paleo-Tethys: Journal of Asian Earth Sciences, v. 32, p. 371–384.

Jian, P., Liu, D., Kröner, A., Zhang, Q., Wang, Y., Sun, X., and Zhang, W., 2009, Devonian to Permian plate tectonic cycle of the Paleo-Tethys Orogen in southwest China (II): Insights from zircon ages of ophiolites, arc/back-arc assemblages and within-plate igneous rocks and generation of the Emeishan CFB province: Lithos, v. 113, p. 767–784.

Keskin, M., Genç, Ş., and Tüysüz, O., 2008, Petrology and geochemistry of post-collisional Middle Eocene volcanic units in north-central Turkey: Evidence for magma generation by slab breakoff following the closure of the northern Neotethys Ocean: Lithos, v. 104, p. 267–305.

Leach, D., Sangster, D., Kelley, K., Large, R.R., Garven, G., Allen, C., Gutzmer, J., and Walters, S., 2005, Sediment-hosted lead-zinc deposits: A global perspective: Economic Geology, v. 100, p. 561–607.

Li, J.-X., Qin, K.-Z., Li, G.-M., Xiao, B., Chen, L., and Zhao, J.-X., 2011, Post-collisional ore-bearing adakitic porphyries from Gangdese porphyry copper belt, southern Tibet: Melting of thickened juvenile arc lower crust: Lithos, v. 126, p. 265–277.

Li, W.C., Zeng, P.S., Hou, Z.Q., and White, N.C., 2011, The Pulang porphyry copper deposit and associated felsic intrusions in Yunnan province, southwest China: Economic Geology, v. 106, p. 79–92.

Liang, H.-Y., Sun, W., Su, W.-C., and Zartman, R.E., 2009, Porphyry copper-gold mineralization at Yulong, China, promoted by decreasing redox potential during magnetite alteration: Economic Geology, v. 104, p. 587–596.

Liu, Y.-S., Gao, S., Jin, S.-Y., Hu, S.-H., Sun, M., Zhao, Z.-B., and Feng, J.-L., 2001, Geochemistry of lower crustal xenoliths from Neogene Hannuoba basalt, North China craton: Implications for petrogenesis and lower crustal composition: Geochimica et Cosmochimica Acta, v. 65, p. 2589–2604.

Lu, Y.F., Chen, K.X., and Zhan, M.G., 1998, Geochemical evidence of exhalative-sedimentary bedded skarn copper deposit, Linong: Mineral Deposits, v. 17, p. 705–708 (in Chinese with English abstract).

——1999, Geochemical evidence of exhalative-sedimentary ore-bearing skarns in Yangla copper mineralization concentrated area, Deqin County, northwestern Yunnan Province: Earth Science, v. 24, p. 298–303 (in Chinese with English abstract).

Lu, Y.-J., Kerrich, R., Kemp, A.I.S., McCuaig, T.C., Hou, Z.-Q., Hart, C.J.R., Li, Z.-X., Cawood, P.A., Bagas, L., Yang, Z.-M., Cliff, J., Belousova, E.A., Jourdan, F., and Evans, N.J., 2013, Intracontinental Eocene-Oligocene porphyry Cu mineral systems of Yunnan, western Yangtze craton, China: Compositional characteristics, sources, and implications for continental collision metallogeny: Economic Geology, v. 108, p. 1541–1576.

Luck, J.M., and Allègre, C.J., 1982, The study of molybdenites through the ^{187}Re-^{187}Os chronometer: Earth and Planetary Science Letters, v. 61, p. 291–296.

Ludwig, 2008, User's manual for Isoplot 3.7: A geochronological toolkit for Microsoft Excel: Berkeley Geochronology Center, Special Publication 4, 76 p.

Lü, B.X., Wang, Z., Zhang, N.D., Duan, J.Z., Gao, Z.Y., Shen, G.F., Pan, C.Y., and Yao, P., 1993, Granitoids in the Sanjiang Region (Nujing-Lancangjiang-Jinshajiang Region) and their metallogenetic specialization: Beijing, Geological Publishing House, 328 p. (in Chinese).

Mao, S., and Duan, Z., 2008, The P, V, T, x properties of binary aqueous chloride solutions up to T= 573K and 100MPa: Journal of Chemical Thermodynamics, v. 40, p. 1046–1063.

Meinert, L.D., 1982, Skarn, manto, and breccia pipe formation in sedimentary rocks of the Cananea mining district, Sonora, Mexico: Economic Geology, v. 77, p. 919–949.

——1992, Skarns and skarn deposits: Geoscience Canada, v. 19, p. 145–162.

——1995, Compositional variation of igneous rocks associated with skarn deposits—chemical evidence for a genetic connection between petrogenesis and mineralization: Mineralogical Association of Canada Short Course Series, v. 23, p. 401–418.

Meinert, L.D., Hefton, K.K., Mayes, D., and Tasiran, I., 1997, Geology, zonation, and fluid evolution of the Big Gossan Cu-Au skarn deposit, Ertsberg district, Irian Jaya: Economic Geology, v. 92, p. 509–534.

Meinert, L.D., Hedenquist, J., Satoh, H., and Matsuhisa, Y., 2003, Formation of anhydrous and hydrous skarn in Cu-Au ore deposits by magmatic fluids: Economic Geology, v. 98, p. 147–156.

Meinert, L., Dipple, G., and Nicolescu, S., 2005, World skarn deposits: Economic Geology, v. 100, p. 299–336.

Metcalfe, I., 2002, Permian tectonic framework and palaeogeography of SE Asia: Journal of Asian Earth Sciences, v. 20, p. 551–566.

——2006, Palaeozoic and Mesozoic tectonic evolution and palaeogeography of East Asian crustal fragments: The Korean Peninsula in context: Gondwana Research, v. 9, p. 24–46.

——2013, Gondwana dispersion and Asian accretion: Tectonic and palaeogeographic evolution of eastern Tethys: Journal of Asian Earth Sciences, v. 66, p. 1–33.

Mo, X.X., Lu, F.X., Shen, S.Y., Zhu, Q.W., Hou, Z.Q., Yang, K.H., Deng, J.F., Liu, X.P., He, C.X., Lin, P.Y., Zhang, B.M., Tai, D.Q., Chen, M.H., Hu, X.S., Ye, S., Xue, Y.X., Tan, J., Wei, Q.R., and Fan, L., 1993, Sanjiang Tethyan volcanism and related mineralization: Beijing, Geological Publishing House, 276 p. (in Chinese).

Mo, X., Yang, K., Wang, L., and Dong, G., 2005, Copper and gold metallogeny in the Tethyan Domain in China: Society for Geology Applied to Mineral Deposits, SGA Meeting, 18th, Mineral Deposit Research: Meeting the Global Challenge, Beijing, China, August 18–21, 2005, Proceedings, p. 1247–1250.

Nakano, T., Yoshino, T., Shimazaki, H., and Shimizu, M., 1994, Pyroxene composition as an indicator in the classification of skarn deposits: Economic Geology, v. 89, p. 1567–1580.

Naney, M.T., 1983, Phase equilibria of rock-forming ferromagnesian silicates in granitic systems: American Journal of Science, v. 283, p. 993–1033.

Ohmoto, H., 1972, Systematics of sulfur and carbon isotopes in hydrothermal ore deposits: Economic Geology, v. 67, p. 551–578.

Ohmoto, H., and Goldhaber, M.B., 1997, Sulfur and carbon isotopes, *in* Barnes, H.L., ed., Geochemistry of hydrothermal ore deposits, 3rd ed.: New York, Wiley, p. 517–611.

Ohmoto, H., and Rye, R.O., 1979, Isotopes of sulphur and carbon, *in* Barnes, H.L., ed., Geochemistry of hydrothermal ore deposits: New York, Wiley, p. 509–567.

O'Neil, J.R., Clayton, R.N., and Mayeda, T.K., 1969, Oxygen isotope fractionation in divalent metal carbonates: Journal of Chemical Physics, v. 51, p. 5547.

Pan, G., Xu, Q., Hou, Z., Wang, L., Du, D., Mo, X., Li, D., Wang, M., Li, X., Jiang, X., and Hu, Y., 2003, Archipelagic orogenesis, metallogenic systems and assessment of the mineral resources along the Nujiang-Lancangjiang-Jinshajiang area in southwestern China: Beijing, Geological Publishing House, 420 p. (in Chinese with English abstract).

Pan, G.T., Wang, L.Q., Li, R.S., Yuan, S.H., Ji, W.H., Yin, F.G., Zhang, W.P., and Wang, B.D., 2012, Tectonic evolution of the Qinghai-Tibet Plateau: Journal of Asian Earth Sciences, v. 53, p. 3–14.

Pan, J.Y., 1999, Ore deposit geochemical characteristics and genesis of the copper polymetallic belt in western Yunnan: Unpublished Ph.D. thesis, Guiyang, China, Institute of Geochemistry, Chinese Academy of Sciences, 90 p. (in Chinese).

Pan, J.Y., Zhang, Q., Ma, D.S., and Li, C.Y., 2000, Stable isotope geochemical characteristics of the Yangla copper deposit in western Yunnan province: Acta Mineralogica Sinica, v. 20, p. 385–389 (in Chinese with English abstract).

Pan, J., Zhang, Q., Ma, D., and Li, C., 2001, Cherts from the Yangla copper deposit, western Yunnan Province: Geochemical characteristics and relationship with massive sulfide mineralization: Science in China Series D: Earth Sciences, v. 44, p. 237–244.

Qu, X.M., Yang, Y.Q., and Li, Y.G., 2004, A discussion on origin of Yangla copper deposit in light of diversity of ore-hosting rock types: Mineral Deposits, v. 23, p. 431–442 (in Chinese with English abstract).

Richards, J.P., 2009, Postsubduction porphyry Cu-Au and epithermal Au deposits: Products of remelting of subduction-modified lithosphere: Geology, v. 37, p. 247–250.

Richards, J.P., Wilkinson, D., and Ullrich, T., 2006, Geology of the Sari Gunay epithermal gold deposit, northwest Iran: Economic Geology, v. 101, p. 1455–1496.

Ridolfi, F., Renzulli, A., and Puerini, M., 2010, Stability and chemical equilibrium of amphibole in calc-alkaline magmas: An overview, new thermobarometric formulations and application to subduction-related volcanoes: Contributions to Mineralogy and Petrology, v. 160, p. 45–66.

Roedder, E., 1984, Fluid inclusions: Reviews in Mineralogy, v. 12, 644 p.

Roedder, E., and Bodnar, R., 1980, Geologic pressure determinations from fluid inclusion studies: Annual Review of Earth and Planetary Sciences, v. 8, p. 263.

Searle, M., 2006, Role of the Red River shear zone, Yunnan and Vietnam, in the continental extrusion of SE Asia: Journal of the Geological Society, v. 163, p. 1025–1036.

Shu, Q., Lai, Y., Sun, Y., Wang, C., and Meng, S., 2013, Ore genesis and hydrothermal evolution of the Baiyinnuo'er zinc-lead skarn deposit, northeast China: Evidence from isotopes (S, Pb) and fluid inclusions: Economic Geology, v. 108, p. 835–860.

Sillitoe, R.H., 1972, A plate tectonic model for the origin of porphyry copper deposits: Economic Geology, v. 67, p. 184–197.

——2010, Porphyry copper systems: Economic Geology, v. 105, p. 3–41.

Smoliar, M.I., Walker, R.J., and Morgan, J.W., 1996, Re-Os ages of group IIA, IIIA, IVA, and IVB iron meteorites: Science, v. 271, p. 1099–1102.

Sterner, S.M., Hall, D.L., and Bodnar, R.J., 1988, Synthetic fluid inclusions. V. Solubility relations in the system NaCl-KCl-H_2O under vapor-saturated conditions: Geochimica et Cosmochimica Acta, v. 52, p. 989–1005.

Todt, W., Cliff, R.A., Hanser, A., and Hofmann, A.W., 1996, Evaluation of a ^{202}Pb-^{205}Pb double spike for high-precision lead isotope analysis: Reading the Isotope Code, v. 95, p. 429–437.

Wang, B.D., Wang, L.Q., Pan, G.T., Yin, F.G., Wang, D.B., and Tang, Y., 2013, U-Pb zircon dating of Early Paleozoic gabbro from the Nantinghe ophiolite in the Changning-Menglian suture zone and its geological implication: Chinese Science Bulletin, v. 58, p. 920–930.

Wang, L.Q., Pan, G.T., Li, D.M., and Xu, T.R., 2002, The Rb-Sr age determinations of the "bimodal" volcanic rocks in the Luchun-Hongponiu Chang superimposed rift basin, Deqin, Yunnan: Tethyan Geology, v. 22, p. 65–71 (in Chinese with English abstract).

Wang, R., Richards, J.P., Hou, Z.Q., Yang, Z., and DuFrane, S.A., 2014a, Increased magmatic water content—the key to Oligo-Miocene porphyry Cu-Mo ± Au formation in the eastern Gangdese belt, Tibet: Economic Geology, v. 109, p. 1315–1339.

Wang, R., Richards, J., Hou, Z., and Yang, Z., 2014b, Extent of underthrusting of the Indian plate beneath Tibet controlled the distribution of Miocene porphyry Cu-Mo ± Au deposits: Mineralium Deposita, v. 49, p. 165–173.

Wang, X.F., Metcalfe, I., Jian, P., He, L.Q., and Wang, C.S., 2000, The Jinshajiang-Ailaoshan suture zone, China: Tectonostratigraphy, age and evolution: Journal of Asian Earth Sciences, v. 18, p. 675–690.

Xiao, L., Qi, H., Pirajno, F., Ni, P.Z., Du, J.X., and Wei, Q.R., 2008, Possible correlation between a mantle plume and the evolution of Paleo-Tethys Jinshajiang Ocean: Evidence from a volcanic rifted margin in the Xiaru-Tuoding area, Yunnan, SW China: Lithos, v. 100, p. 112–126.

Xu, L.L., Bi, X.W., Hu, R.Z., Zhang, X.C., Su, W.C., Qu, W.J., Hu, Z.C., and Tang, Y.Y., 2012, Relationships between porphyry Cu-Mo mineralization in the Jinshajiang-Red River metallogenic belt and tectonic activity: Constraints from zircon U-Pb and molybdenite Re-Os geochronology: Ore Geology Reviews, v. 48, p. 460–473.

Xu, X.-W., Cai, X.-P., Xiao, Q.-B., and Peters, S.G., 2007, Porphyry Cu-Au and associated polymetallic Fe-Cu-Au deposits in the Beiya area, western Yunnan Province, south China: Ore Geology Reviews, v. 31, p. 224–246.

Yang, X.A., 2012, Superimposition mineralization and exploring model in the Yangla metallogenic belt, western Yunnan: Unpublished Ph.D. thesis, Beijing, China, China University of Geosciences (Beijing), 147 p. (in Chinese).

Yin, A., and Harrison, T.M., 2000, Geologic evolution of the Himalayan-Tibetan Orogen: Annual Review of Earth and Planetary Sciences, v. 28, p. 211–280.

Zaw, K., Peters, S.G., Cromie, P., Burrett, C., and Hou, Z., 2007, Nature, diversity of deposit types and metallogenic relations of south China: Ore Geology Reviews, v. 31, p. 3–47.

Zhan, M.G., Lu, Y.F., Chen, S.F., Dong, F.L., Chen, K.X., Wei, J.Q., He, L.Q., Huo, X.S., Gan, J.M., and Yu, F.M., 1998, Deqin Yangla copper deposit in western Yunnan Province: Wuhan, China University of Geology Publishing House, 163 p. (in Chinese).

Zhong, D.L., 2000, Paleotethys sides in west Yunnan and Sichuan, China: Beijing, Science Press, 248 p. (in Chinese with English abstract).

Zhu, J., Li, W.C., Zeng, P.S., Yin, G.H., Wang, Y.B., Wang, Y., Yu, H.J., Dong, T., and Hu, Y.B., 2011, Geological and geochemical evidences of compound genesis of Yangla bedded copper deposit, northwestern Yunnan: Geological Review, v. 57, p. 337–349 (in Chinese with English abstract).

Zhu, J.-J., Hu, R.-Z., Bi, X.-W., Zhong, H., and Chen, H., 2011, Zircon U-Pb ages, Hf-O isotopes and whole-rock Sr-Nd-Pb isotopic geochemistry of granitoids in the Jinshajiang suture zone, SW China: Constraints on petrogenesis and tectonic evolution of the Paleo-Tethys Ocean: Lithos, v. 126, p. 248–264.

Zhu, X., Mo, X., White, N.C., Zhang, B., Sun, M., Wang, S., Zhao, S., and Yang, Y., 2013, Petrogenesis and metallogenic setting of the Habo porphyry Cu-(Mo-Au) deposit, Yunnan, China: Journal of Asian Earth Sciences, v. 66, p. 188–203.

Zi, J.W., Cawood, P.A., Fan, W.M., Wang, Y.J., and Tohver, E., 2012a, Contrasting rift and subduction-related plagiogranites in the Jinshajiang ophiolitic mélange, southwest China, and implications for the Paleo-Tethys: Tectonics, v. 31, p. 1–18.

Zi, J.-W., Cawood, P.A., Fan, W.-M., Wang, Y.-J., Tohver, E., McCuaig, T.C., and Peng, T.-P., 2012b, Triassic collision in the Paleo-Tethys Ocean constrained by volcanic activity in SW China: Lithos, v. 144–145, p. 145–160.

Zi, J.-W., Cawood, P.A., Fan, W.-M., Tohver, E., Wang, Y.-J., and McCuaig, T.C., 2012c, Generation of Early Indosinian enriched mantle-derived granitoid pluton in the Sanjiang Orogen (SW China) in response to closure of the Paleo-Tethys: Lithos, v. 140–141, p. 166–182.

Zi, J.-W., Cawood, P.A., Fan, W.-M., Tohver, E., Wang, Y.-J., McCuaig, T.C., and Peng, T.-P., 2013, Late Permian-Triassic magmatic evolution in the Jinshajiang orogenic belt, SW China and implications for orogenic processes following closure of the Paleo-Tethys: American Journal of Science, v. 313, p. 81–112.